Plasmodium falciparum impairs Ang-1 secretion by pericytes in a 3D brain microvessel model

Rory K. M. Long[1,2], François Korbmacher[1], Paolo Ronchi[3], Hannah Fleckenstein[1,3], Martin Schorb[3], Waleed Mirza[1], Mireia Mallorquí[1], Ruth Aguilar[4], Gemma Moncunill[4], Yannick Schwab[3], Maria Bernabeu[1]*

[1]European Molecular Biology Laboratory (EMBL) Barcelona, Barcelona, Spain

[2]Heidelberg University, Faculty of Biosciences, Heidelberg, Germany

[3]European Molecular Biology Laboratory (EMBL), Cell Biology and Biophysics Unit, Heidelberg, Germany.

[4]Barcelona Institute for Global Health (ISGlobal), Hospital Clínic-Universitat de Barcelona, Barcelona, Spain

*To whom correspondence should be addressed. Email: maria.bernabeu@embl.es

Maria Bernabeu
EMBL Barcelona
Dr. Aiguader 88
Barcelona, Spain, 08003
maria.bernabeu@embl.es

The authors declare that they do not have any conflict of interest.

Abstract

Disruption of the vascular protective angiopoietin-Tie axis is common in cerebral malaria (CM) patients, who display elevated angiopoietin-2 (Ang-2) and reduced angiopoietin-1 (Ang-1) blood concentrations. The role of pericytes in CM pathogenesis remains unexplored, despite being a major source of brain Ang-1 secretion and evidence of pericyte damage observed in CM postmortem samples. Here we engineered a human 3D microfluidics-based brain microvessel model containing the minimal cellular components to replicate the angiopoietin-Tie axis, human primary brain microvascular endothelial cells and pericytes. This model replicated pericyte vessel coverage and ultrastructural interactions present in the brain microvasculature. When exposed to *P. falciparum*-iRBC egress products, 3D brain microvessels presented decreased Ang-1 secretion, increased vascular permeability, and minor ultrastructural changes in pericyte morphology. Notably, *P. falciparum*-mediated barrier disruption was partially reversed after pre-treatment with recombinant Ang-1 and the Tie-2 activator, AKB-9778. Our approach suggests a novel mechanistic role of pericytes in CM pathogenesis and highlights the potential of therapeutics that target the angiopoietin-Tie axis to rapidly counteract vascular dysfunction caused by *P. falciparum*.

The paper explained

Problem

Cerebral malaria (CM) is a severe complication of *Plasmodium falciparum* infection, resulting in the majority of ~600000 malarial deaths annually. Despite anti-malarial drug administration upon hospitalization, fatality rates still range from 15-25% and many survivors suffer long term neurological disabilities. A common dysregulated vascular pathway identified in CM patients is the angiopoietin-Tie axis. Treatments that restore this vascular homeostatic pathway appear as a potential avenue for adjunctive therapies in experimental rodent CM models. Nevertheless, the use of rodent CM models for therapeutic discovery is not ideal, given that *P. falciparum* pathogenesis is species-specific. Therefore, the development of novel and advanced human 3D microvascular models offers new avenues to study disease pathogenesis and explore potential adjunctive CM treatments.

Results

In this study, we generate a 3D human brain microvasculature model that reproduces *in vivo* interactions between two key cell types necessary to reproduce the protective angiopoietin-Tie axis: human brain endothelial cells and pericytes. Addition of *P. falciparum*-infected red blood cell (iRBC) egress products causes vascular disruption and hampers the release of the vascular protective factor, angiopoietin-1, from brain pericytes. 18-hour pre-treatment of Ang-1 for 18h prevents iRBC egress product-induced vascular disruption. A short pre-treatment of the microvessels with AKB-9778, a downstream pharmaceutical inducer of angiopoietin-Tie axis activity currently in phase II clinical trial for diabetic retinopathy, partially restores vascular integrity. Our study highlights the role of pericytes in CM and the therapeutic potential of interventions that restore the angiopoietin-Tie2 axis as adjunctive CM treatments.

Impact

Our study demonstrates the potential of bioengineered vascular models to recapitulate dysregulated pathways previously characterized in malaria patients, and in providing a physiologically-relevant platform to test adjunctive therapies. The use of the 3D brain microvascular model has enhanced our understanding of the mechanisms behind CM pathogenesis, uncovering a previously unappreciated effect of *P. falciparum* on brain pericytes, linking angiopoietin-Tie axis dysregulation and microvasculature disruption. These findings pave the way for the identification of novel, fast-acting therapeutics, such as AKB-9778, to restore vascular integrity in CM patients.

Introduction

Cerebral malaria (CM) is a severe neurological complication of *Plasmodium falciparum* infection, clinically characterized by coma and fatality rates averaging 15-20% (Dondorp *et al*, 2010). Furthermore, approximately one third of CM survivors endure lifelong neurological sequelae such as hemiplegia, ataxia, epilepsy or speech disorders (Birbeck *et al*, 2010). The majority of pediatric CM-related deaths present severe brain swelling due to vasogenic edema, likely as a consequence of blood-brain barrier dysfunction (Mohanty *et al*, 2017). A hallmark of CM is the sequestration of *P. falciparum*-infected red blood cells (iRBC) in the brain microvasculature (Dorovini-Zis *et al*, 2011). While the molecular players responsible for *P. falciparum*-iRBC ligand-receptor interactions with cerebral endothelial cells have been extensively studied (Kessler *et al*, 2017; Storm *et al*, 2019; Sahu *et al*, 2022), the consequences of iRBC sequestration in the brain microvasculature require further investigation. Nevertheless, evidence suggests that increases in vascular permeability during CM are a result of a multifaceted process including the blockade of barrier-supportive endothelial receptors by iRBC, the release of toxic *P. falciparum* products from egressed iRBC, and a dysregulated host innate immune response (Bernabeu & Smith, 2017; Wassmer *et al*, 2024).

An important pathway commonly dysregulated in CM patients is the angiopoietin-Tie axis, crucial to maintaining endothelial pro-barrier, anti-inflammatory, and anti-apoptotic functions (Augustin *et al*, 2009). Binding of the ligand angiopoietin-1 (Ang-1) to the endothelial receptor Tie-2 promotes vascular quiescence and the stabilization of endothelial tight junction proteins, such as Occludin and Zona Occludens-1 (ZO-1), necessary for maintaining the barrier function of the brain microvasculature (Fukuhara *et al*, 2008; Saharinen *et al*, 2008; Siddiqui *et al*, 2015). Conversely, angiopoietin-2 (Ang-2), which is rapidly released from small endothelial storage granules called Weibel-Palade bodies, generally acts as a Tie-2 antagonist leading to endothelial activation and vascular leakage (Maisonpierre *et al*, 1997). Given the opposing roles of these two molecules in vascular function, increased levels of Ang-2 and decreased levels of Ang-1 have been largely associated with cerebral vascular pathogenesis in a multitude of diseases (Gurnik *et al*, 2016; Golledge *et al*, 2014). Similarly, a decrease in Ang-1, and an increase in Ang-2 and the Ang-2:Ang-1 ratio has been well documented in fatal cases of both pediatric and adult CM (Yeo *et al*, 2008; Lovegrove *et al*, 2009; Conroy *et al*, 2009, 2012; Jain *et al*, 2011). Despite its importance, the mechanisms leading to angiopoietin-Tie axis disruption in CM are poorly understood. Human pro-inflammatory cytokines and pro-coagulation proteins, such as TNF-α and thrombin, have been proposed to be responsible for the increase of Ang-2 secretion by endothelial cells (Gomes *et al*,

111 2023; Fiedler *et al*, 2004), but the causative agent responsible for decreased secretion of Ang-1 in
112 CM patients remains unknown.

113 Vascular mural cells, including smooth muscle cells and pericytes are the main cellular sources for
114 Ang-1 secretion in the brain microvasculature (Augustin *et al*, 2009). Beyond promoting
115 endothelial barrier function through Ang-1 secretion, pericytes support the microvasculature and
116 promote quiescence through additional roles. Structurally, pericytes wrap around cerebral
117 microvessels and interact with the endothelium through reciprocal ultrastructural membrane
118 protrusions, known as peg-and-socket junctions (Ornelas *et al*, 2021), and secrete extracellular
119 matrix components of the basal lamina that strengthen microvascular architecture. Functionally,
120 pericytes regulate brain blood flow by controlling vessel diameter through constriction (Daneman
121 & Prat, 2015). Cerebral pericytes have been implicated in various vascular disorders of the central
122 nervous system. Loss of pericytes from the cerebral vasculature during ischemic stroke and
123 Alzheimer's disease is associated with brain microvascular disruption, extravasation of blood
124 components into the brain parenchyma, and neuronal loss (Fernández-Klett *et al*, 2013; Sengillo *et*
125 *al*, 2013). Similarly, histopathological studies in retinal samples of fatal pediatric CM cases have
126 revealed pericyte damage in regions of iRBC sequestration, suggesting a similar role of these cell
127 types in severe malaria infections (Barrera *et al*, 2018). Yet, the role of cerebral pericytes in CM
128 pathogenesis and in the dysregulation of the angiopoietin-Tie pathway remains largely unknown.
129 Bioengineered vascular models are emerging as powerful tools to study disease mechanisms *in*
130 *vitro.* They have been successfully used to recapitulate important vascular pathways, including the
131 role of pericytes and the angiopoietin-Tie axis in the establishment of vascular networks (Haase *et*
132 *al*, 2019), and more recently, malaria pathogenesis, by modeling ligand-receptor interaction of
133 iRBC in microvessels (Bernabeu *et al*, 2019) or parasite-induced endothelial stress and
134 inflammatory response (Howard *et al*, 2023). Here, we have developed a 3D brain microvascular
135 model composed of primary brain endothelial cells and pericytes that recapitulates the minimal
136 functional cellular unit of the angiopoietin-Tie axis found in the *in vivo* human brain. We have used
137 this model to understand the interplay between iRBC, brain endothelial cells and pericytes that
138 contributes to the molecular basis of angiopoietin-Tie dysregulation in CM. Our results indicate
139 that products released during iRBC egress play a role in angiopoietin-Tie dysregulation by
140 decreasing Ang-1 secretion by pericytes, highlighting the role of this cell type as a new player in
141 CM pathogenesis. Furthermore, we showed that parasite-induced increase in endothelial
142 permeability can be therapeutically targeted by the use of the angiopoietin-Tie axis inducers, such
143 as the Tie-2 activator AKB-9778.

Results

In vitro 3D brain microvessel model recapitulates *in vivo* cerebral endothelial-pericyte interactions

Primary human brain microvascular endothelial cells (HBMEC) and human brain vascular pericytes (HBVP) were commercially purchased and the expression of cell type-specific markers was validated, including junctional proteins and transporters: vascular endothelial (VE)-cadherin, β-catenin, zonula occludens-1 (ZO-1), claudin-5 and glucose transporter-1 (GLUT-1), as well as, endothelial specific markers: CD31 and von Willebrand Factor (vWF) for HBMEC (Fig. EV1A,B). HBVP expressed brain pericyte markers platelet derived growth factor receptor β (PDGFRβ) and nerve/glial antigen 2 (NG-2) (Fig. EV1C) (He *et al*, 2016; Attwell *et al*, 2016). Furthermore, we confirmed HBMEC secretion of Ang-2 and Ang-1 exclusively secreted by HBVP in a transwell model (Fig. EV1D). To better recapitulate the brain microvascular architecture, we have generated a 3D brain microvessel model that recapitulates the minimal functional cellular unit of the angiopoietin-Tie axis. The device is fabricated in a collagen type I hydrogel containing a microfluidic network with a pre-defined geometry, which is connected to both an inlet and outlet, enabling vessel perfusion (Zheng *et al*, 2012). Previous incorporation of pericytes in similar bioengineered 3D models involved cellular addition into the collagen hydrogel itself. However, this resulted in sparse interaction of pericytes with the endothelial microvessels (Zheng *et al*, 2012). Nevertheless, *in vivo* cerebral pericytes have been shown to cover approximately one third of the brain microvasculature, albeit with slight variations along the brain vascular hierarchical network (Mathiisen *et al*, 2010; Uemura *et al*, 2020). To recreate this, HBVP were seeded directly into the channels along with HBMEC at a 5:1 endothelial to pericyte ratio (Fig. 1A). After 3 days in culture, the two cell types reorganized into two different layers with HBMEC forming a network of 100-µm diameter microvessels and mCherry-expressing HBVP covering the microvessel surface (Fig. 1B). HBVP distributed homogenously around the vessel cross-section, covering approximately a third of the microvessel surface area (29.6% of the bottom surface and 27.3% of the top surface) (Fig. 1C). Endothelial VE-cadherin junctional labeling is continuous along the vessel luminal surface, suggesting that the presence of HBVP does not disrupt the endothelial layer (Fig. 1D). Furthermore, HBMEC in the model retain the expression of endothelial adherens and tight junction markers, β-catenin and ZO-1 respectively (Fig. 1E). HBVP keep the expression of pericyte markers PDGFRβ and NG-2, as well as the mural cell contractile protein α-smooth muscle actin (αSMA), and appear as elongated cells with thin processes stretching over multiple endothelial cells (Fig. 1D, E). In addition, HBVP secrete laminin and collagen IV, contributing to the secretion of

extracellular matrix components that compose the basal lamina of brain microvasculature *in vivo* (Fig. 1E) (Oliveira *et al*, 2023).

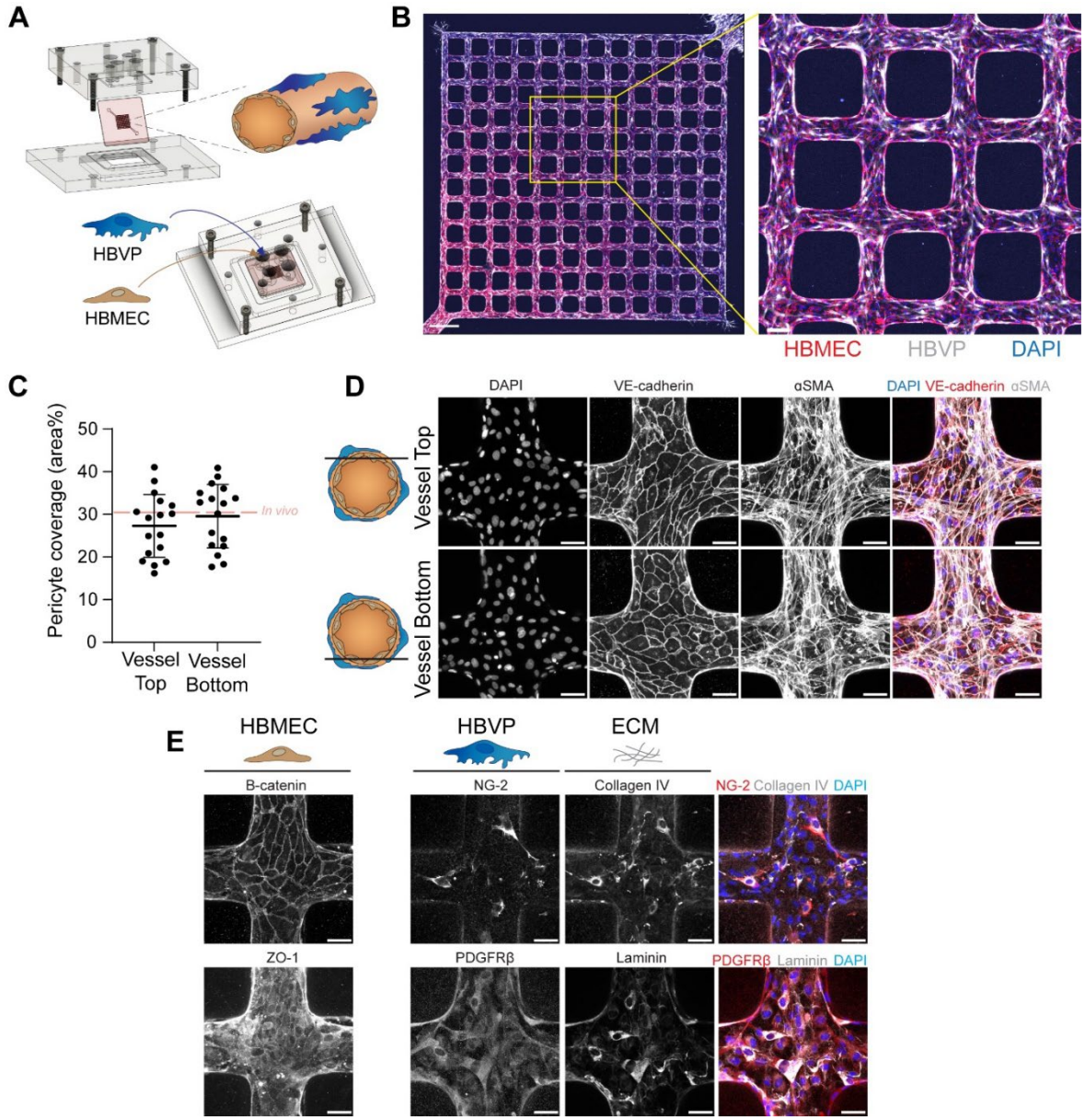

Figure 1 - Generation and characterization of a 3D brain microvasculature model.
A Schematic depiction of the fabrication pieces and device set-up (top-left), including a representation of resultant endothelial-pericyte interactions (top-right), and the seeding method used to generate the 3D microvessel model (bottom).
B Immunofluorescence assay (IFA) maximum z-projection of the full network of cellularized channels labeled with Von-Willebrand factor for HBMEC (red), mCherry-expressing HBVP (white) and DAPI (blue) (left). Inset highlighting pericyte coverage of the microvessels (right). Scale bars: 500 µm and 100 µm (Inset).
C Quantification of the percentage of endothelial microvessel area covered by pericytes on either the top or bottom microvessel surface in a z cross-sectional view. Red dashed line represents

191 estimated *in vivo* brain microvascular pericyte coverage. Data is presented as mean +/- standard
192 deviation (n = 17 devices, Mann-Whitney U test).
193 **D** IFA maximum z-projection of VE-cadherin, αSMA, and DAPI labeling on the top and bottom
194 cross-sectional surfaces of microvessels (left). Merged maximum z-projections with VE-cadherin
195 (red), αSMA (white) and DAPI (blue) (right). Scale bar: 50 µm.
196 **E** IFA maximum z-projection of brain endothelial markers, ZO-1 and β-catenin, as well as,
197 colocalization between brain pericyte markers, NG-2 and PDGFRβ (red), and extracellular matrix
198 markers, laminin and collagen IV (grey) in the presence of DAPI staining (blue). Scale bar: 50 µm.
199

200 Volumetric electron microscopy has been previously used to characterize *in vivo* 3D ultrastructural
201 interactions between pericytes and endothelial cells of the cerebral microvasculature (Ornelas *et al*,
202 2021). To characterize the spatial and ultrastructural organization of pericytes and endothelial cells
203 in the model, we utilized Serial Block-Face Scanning Electron Microscopy (SBF-SEM) (Denk &
204 Horstmann, 2004), a volume electron microscopy technique that provides nanoscale resolution of
205 samples in a large field of view (Peddie *et al*, 2022). We imaged a 100 µm segment of a microvessel
206 branch with a 15x15x50 nm xyz resolution, followed by cellular segmentation and rendering. We
207 characterized the spatial distribution and morphology of approximately 25 individual HBVP,
208 distinguished from HBMEC by the presence of a highly granulated cytoplasm (Nahirney *et al*,
209 2016). Cross-sectional analysis and segmentation of the microvessel revealed an ovoid microvessel
210 morphology, and confirmed the presence of HBVP at the abluminal side of the HBMEC (Fig. 2A).
211 HBVP acquired a classical bump-on-a-log morphology, with the soma being the thickest region of
212 the cell, and their longitudinal axis aligned with the direction of flow (Fig. 2B). Most of the
213 HBMEC-HBVP interface is composed of thin pericytic lamellae (100-300 nm thickness) that cover
214 large areas of the endothelial surface, with multiple thin branches appearing mostly at the pericyte
215 periphery, as described previously (Ornelas *et al*, 2021). A close up of regions of HBVP-HBMEC
216 cell interaction reveal that the membranes of both cell types are in close proximity (Fig. 2C).
217 Pericytes in the brain constitute a heterogenous cell population depending on their location within
218 the vascular branch. Considering the arteriole-sized diameter (100 µm) of the microvessels, the co-
219 expression of αSMA, PDGFRβ and NG-2 staining, and the bump-on-a-log morphology, HBVP
220 within the model are reminiscent of ensheathing pericytes, commonly found on cerebral arterioles
221 rather than capillary pericytes that appear not to express αSMA (Smyth *et al*, 2018; Grant *et al*,
222 2019). Overall, the 3D *in vitro* brain microvessel model recapitulates *in vivo* interactions between
223 brain endothelial cells and pericytes, both at the tissue and ultrastructural level, that can next be
224 utilized to model the role of pericytes in malaria pathogenesis.

225

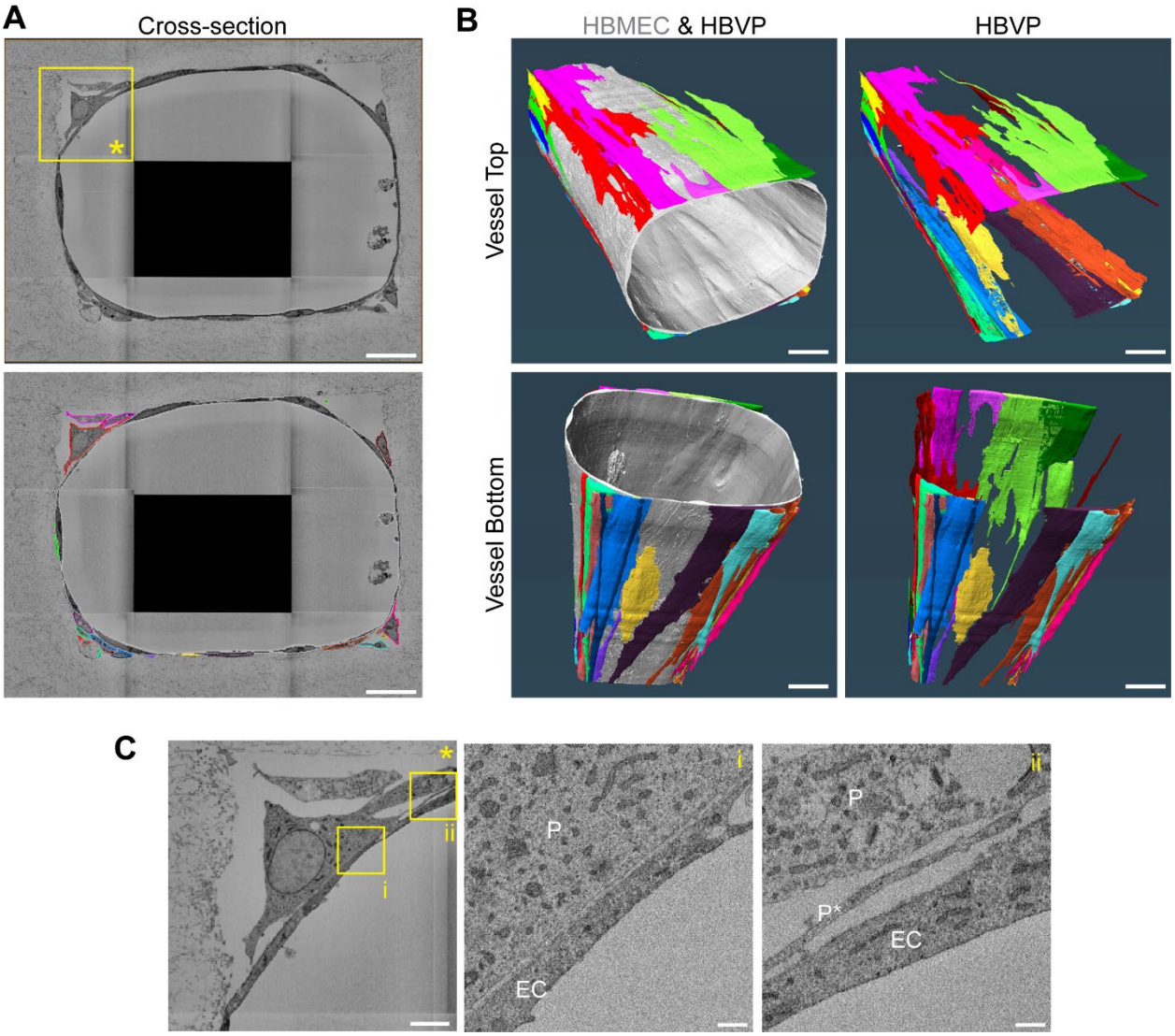

Figure 2 - Serial block-face scanning electron microscopy reveals endothelial cell-pericyte ultrastructural interactions.

A Cross-section of the microvessel imaged through the SBF-SEM volume (top) and the corresponding segmentation outlines of the endothelium (grey) and surrounding pericytes (coloured). Scale bar: 20 µm.

B 3D rendering of the segmented microvessel (grey) and the surrounding pericytes viewed from above or below. Scale bar: 10 µm.

C Zoomed images of the region of interest (ROI) in A. Insets show ROIs i and ii where pericytes are denoted with "P", endothelial cells by "EC" and pericyte lamellae by "P*". Scale bars: 5 µm (left) and 500 nm (center and right).

239 ***P. falciparum* egress products increase vessel permeability but only cause minor changes in**
240 **pericyte morphology**
241 *In vitro* studies have shown that *P. falciparum* products released during malaria parasite egress
242 disrupt the endothelial barrier (Gillrie *et al*, 2007; Gallego-Delgado *et al*, 2016; Pal *et al*, 2016;
243 Storm *et al*, 2019; Moxon *et al*, 2020). To characterize the impact that these could have on pericyte
244 function, we established a protocol to create media enriched for *P. falciparum*-iRBC egressed
245 products, denoted from here on as iRBC-egress media. Briefly, tightly synchronized schizont stage-
246 iRBC were purified and allowed to egress in vascular growth media, followed by recovery of the
247 supernatant fraction containing *P. falciparum* soluble products at an estimated concentration of
248 $5x10^7$ ruptured iRBC/mL (equivalent to simultaneous egress of parasites at a parasitemia of
249 approximately 1%) (Fig. EV2A, B). We measured the endothelial disruptive properties of iRBC-
250 egress media by the xCELLigence system, which provides real time measurement of cell barrier
251 integrity through impedance. Incubation with *P. falciparum* egress products caused a significant,
252 dose-dependent decrease in cell index, a measurement of monolayer barrier function normalized to
253 untreated cells, reaching a maximum disruption at 18 hours (Fig. EV2C). To elucidate if iRBC-
254 egress media also induces barrier breakdown in the brain 3D microvessel model, we performed
255 permeability assays in a simpler microvessel network which consists of a single 200 µm channel.
256 After perfusion and incubation with iRBC-egress media for 18 hours, *P. falciparum* egress products
257 accumulated on the walls of the microvessel channel and appeared as dark spots in brightfield
258 suggesting the presence of parasitic hemozoin and food vacuoles (Fig. 3A). Microvessels perfused
259 with iRBC-egress media presented a significant increase to 70 kDa FITC-dextran permeability
260 across the entire vessel wall, corresponding to a 6-fold increment compared to vessels perfused with
261 vascular cell media ($4.08x10^{-6}$ cm/s in media-only vs. $2.66x10^{-5}$ cm/s in devices exposed to iRBC-
262 egress media) (Fig. 3A, B). Although the presence of inter-endothelial gaps was not observed, VE-
263 cadherin staining revealed areas of discontinuity and thinning of adherens junctions in regions
264 nearby the deposition of parasitic DAPI-positive DNA remnants (Fig. 3C).

265 To determine whether increased permeability was associated with physical changes in pericytes,
266 we assessed their cellular morphology in 3D microvessels exposed to iRBC-egress media for 18-
267 hours by SBF-SEM. HBVP maintained close spatial proximity to the endothelium in the presence
268 of *P. falciparum*-iRBC ghosts, similar to control devices exposed to vascular growth media (Fig.
269 3D). To investigate potential changes in HBVP shape, we isolated and analyzed each 3D rendered
270 HBVP (Figs. 3E,F and EV3A,B). Cellular features such as circularity and maximum width did not
271 differ between conditions, however, iRBC-egress media treated HBVP presented fewer branches
272 suggesting a response to iRBC-egress media (Fig. 3E,F). Altogether, our results show that *P.*

falciparum egress products cause an increase in permeability of the 3D brain microvessel model, accompanied by minor changes in pericyte morphology.

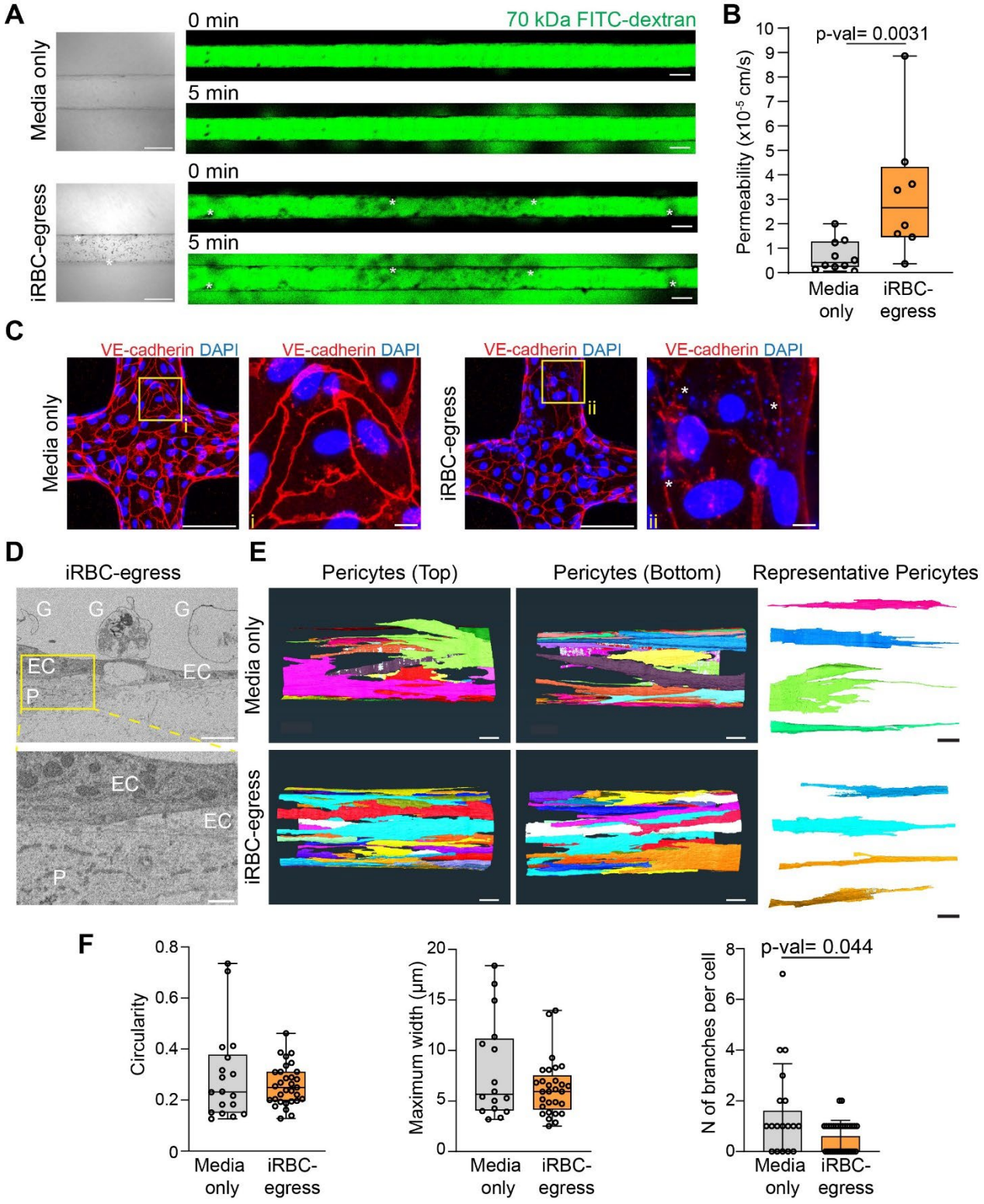

Figure 3 - iRBC egress products increase microvessel permeability with minor changes in pericyte morphology.

A Brightfield images of 3D brain microvessel channels after 18-hour incubation with media only or iRBC-egress media (left). Scale bar: 200 µm. Representative confocal images of 70 kDa FITC-dextran flux into the surrounding collagen 0 and 5 minutes after perfusion (right). Scale bar: 200 µm. Accumulated *P. falciparum*-iRBC egress material is represented with asterisks.
B Apparent permeability of 70 kDa FITC-dextran in channels treated with media only or *P. falciparum*-iRBC egress media for 18-hours. (n = 8 individual devices).
C Immunofluorescence maximum z-projection of 3D brain microvessels exposed to media only or iRBC-egress media stained with VE-cadherin (red) and DAPI (blue). Insets show ROIs of i and ii that display adherens junctions in the presence of cytoadhered DAPI-positive iRBC egress products represented by asterisks. Scale bar: 100 µm and 10 µm in insets.
D SBF-SEM image and zoomed ROI of microvessels treated with iRBC-egress media. Pericytes are denoted as "P", endothelial cells by "EC" and iRBC ghosts by "G". Scale bar: 2 µm (top) and 500 nm in inset (bottom).
E 3D rendering of pericytes segmented from microvessels treated with media only or iRBC-egress media and imaged with SBF-SEM (left). Scale bar: 10 µm. Representative segmented pericytes for morphology analysis (right). Scale bar: 10 µm.
F Circularity, maximum width and number (N) of branches analysis (n = 18 or 31 segmented pericytes treated with media only or iRBC-egress media respectively).
Data information: In **B** and **F** data are presented as box and whisker plots displaying the median, 25th and 75th percentiles and the minimum and maximum data points (Mann-Whitney U test).

P. falciparum-iRBC induce dysregulation of the angiopoietin-Tie axis

Next, we aimed to determine whether parasite egress products are a major driver of angiopoietin-Tie axis disruption characteristic of CM (Yeo *et al*, 2008; Lovegrove *et al*, 2009; Conroy *et al*, 2009, 2012; Higgins *et al*, 2016). A multiplexed Luminex assay was used to measure secreted protein concentrations in microvessel supernatants recovered after 18-hour incubation with iRBC-egress media. Remarkably, we observed a substantial decline of Ang-1 secretion by HBVP following iRBC-egress media incubation (Fig. 4A). Consistent with recent studies on 2D HBMEC monolayers (Gomes *et al*, 2023), iRBC-egress media incubation did not result in increased Ang-2 secretion. Indeed, we quantified a significant decrease in Ang-2 secretion (Fig. 4A). Despite Ang-2 decrease, a significant increase in the Ang-2:Ang-1 ratio was found (Fig. 4A). Additionally, we observed a decrease in 3D microvessel secretion or shedding of other vascular factors important for endothelial-pericyte interaction, such as Neural cadherin (N-cadherin) and Tissue Inhibitor of Metalloproteinase-1 (TIMP-1) (Fig.EV4A). Conversely, we detected no changes in soluble Vascular Endothelial Growth Factor (VEGF), Tie-2, Angiopoietin-like-4 (ANGPTL4), Platelet Derived Growth Factor-BB (PDGF-BB), Interleukin-8 (IL-8) or Chemokine Ligand-1 (CXCL-1) after 18-hour incubation with iRBC-egress media (Fig. EV4).

To validate whether changes in the angiopoietin-Tie axis occur physiologically following *P. falciparum* blood stage egress within the microvasculature, we perfused the 3D brain microvessels

with schizont stage *P. falciparum*-iRBC for 30 minutes followed by a 10-minute wash. After an 18-hour incubation period, supernatants were again recovered and analyzed by Luminex. Similar results were obtained, with a reduction in both Ang-1 and Ang-2 secretion and an increase in the Ang-2:Ang-1 ratio (Fig. 4B). Altogether, these results suggest that *P. falciparum*-iRBC hamper Ang-1 secretion by pericytes, revealing a previously unappreciated role of pericytes in the dysregulation of the angiopoietin-Tie axis in CM.

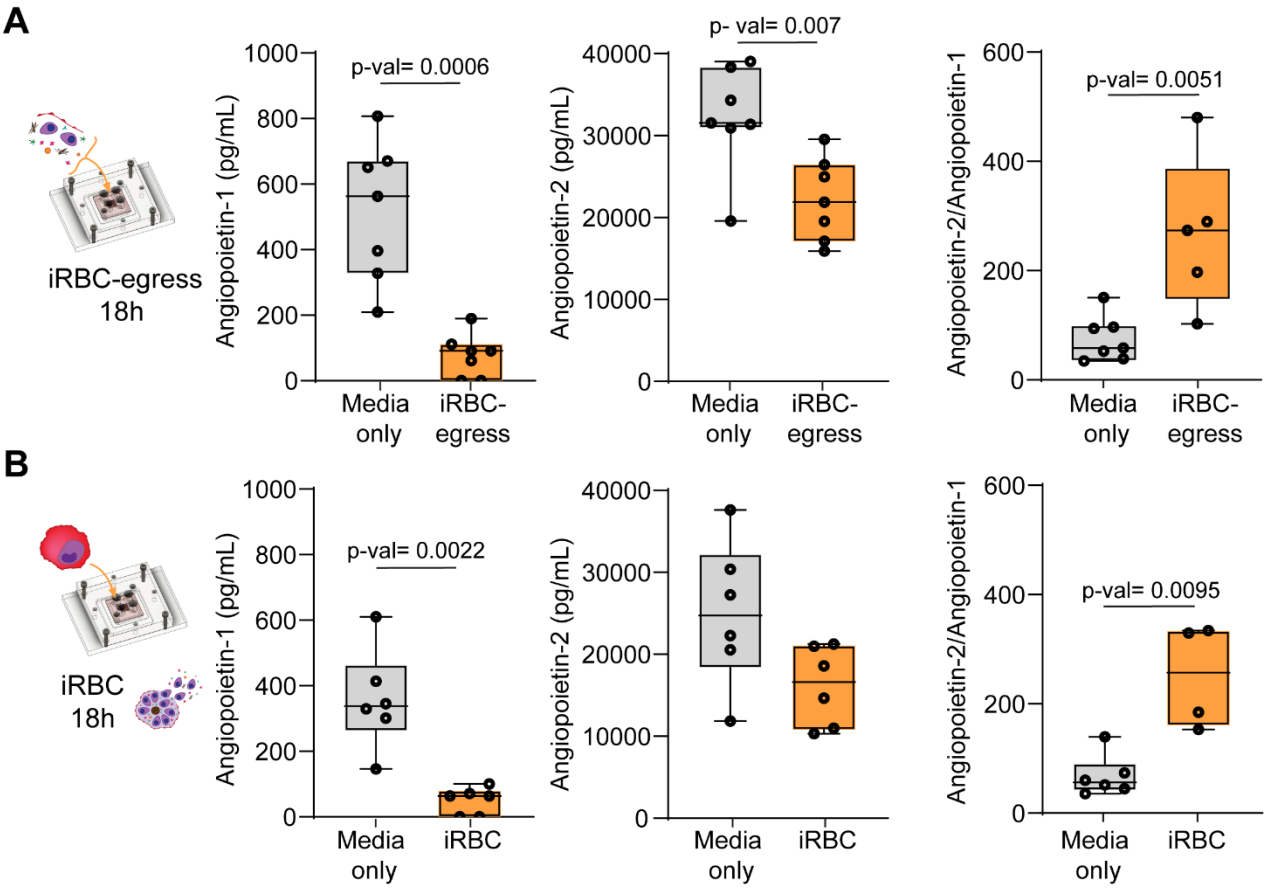

Figure 4 - iRBC egress products induce angiopoietin-Tie axis dysregulation by altering pericyte secretion of Ang-1.

A, B Ang-1, Ang-2 concentrations, and Ang-2: Ang-1 ratio measured from 3D brain microvessels treated with media only, iRBC-egress media (A) or *P. falciparum*-iRBC (B) for 18-hours (n = 6-7 pooled supernatants from 2-3 devices each)

Data information: Box and whisker plots display the median, 25th and 75th percentiles and the minimum and maximum data points (Mann-Whitney U test) In **A** and **B**, data points in which Ang-1 concentrations were below the limit of detection were removed to calculate the Ang-2: Ang-1 ratio.

335 **Therapeutic targeting of the angiopoietin-Tie axis partially protects against endothelial**
336 **barrier breakdown by iRBC-egress media**

337 Currently, there are no available host-targeted adjunctive therapies to restore cerebral vascular
338 barrier function during CM. Given the key role of Ang-1 in promoting vascular quiescence and
339 endothelial barrier formation we first investigated whether recombinant Ang-1 (rAng-1)
340 supplementation could protect against the barrier disruptive effects of iRBC-egress media. First,
341 we measured barrier disruption by xCELLigence in a 2D *in vitro* HBMEC culture in the absence
342 of HBVP. An 18-hour pre-treatment of rAng-1 prior to HBMECexposure to iRBC-egress partially
343 protected against parasite-mediated endothelial barrier disruption, while an 1-hour pre-treatment
344 did not display a protective effect (Fig. EV5A-F). The 18-hour pre-treatment with rAng-1 conferred
345 a 40% barrier breakdown protection after normalization to the untreated endothelial condition (Fig.
346 EV5F). Next, we tested the protective capacity of rAng-1 against iRBC-egress products in the 3D
347 microvessel model (Fig. 5A). Microvessels pretreated with rAng-1 did not present a significant
348 increase in 70 kDa FITC-dextran permeability when exposed to iRBC-egress media. While vessels
349 exposed to iRBC-egress media presented a median 6.4-fold increase in permeability, iRBC-egress
350 vessels pre-treated with Ang-1 only presented a 1.3-fold increase in permeability compared to the
351 rAng-1 treated control, equivalent to a 80% recovery in barrier breakdown (Fig. 5B,C). Taken
352 together, pre-treatment with rAng-1 protects against the microvascular permeability caused by
353 iRBC egress products, showing the potential for vascular restorative pathways that target the
354 angiopoietin-Tie2 axis in CM treatment while highlighting the importance that a decrease in Ang-
355 1 could have in CM-induced vascular disruption.
356 During angiogenesis, vascular endothelial-protein tyrosine phosphatase (VE-PTP) regulates Tie-2
357 activity by dephosphorylation (Fachinger et al., 1999). AKB-9778, a pharmacological inhibitor of
358 VE-PTP activity, has been shown to specifically activate the angiopoietin-Tie axis to promote
359 endothelial barrier function in the presence of various mediators of vascular disruption and
360 inflammation (Shen et al., 2014; Frye et al., 2015). Therefore, AKB-9778 is currently undergoing
361 phase II clinical trials as a therapeutic treatment for retinal vascular diseases characterized by
362 angiopoietin-Tie axis dysregulation such as diabetic retinopathy (Sha et al., 2024). As the retinal
363 and brain vasculature share similar embryological origin, anatomy, cell composition and response
364 during CM (Patton et al., 2005; MacCormick et al., 2014), we tested the potential of AKB-9778 as
365 a therapeutic option to counteract CM. In a 2D *in vitro* HBMEC culture, both 1- and 18-hour pre-
366 treatment with AKB-9778 resulted in a partial protection against parasite-mediated endothelial
367 barrier disruption of 56% and 43%, respectively (Fig. EV6A-F). Given the ability of AKB-9778 to

protect against barrier disruption in 2D monolayers, we next validated its rapid protective activity in the 3D microvessel model (Fig. 5D). Microvessels pre-treated for 1h with AKB-9778 and exposed to iRBC-egress media presented a non-significant ~2-fold increase in permeability while untreated microvessels presented a significant 3.2-fold increase in permeability, representing a 39% decrease in microvessel leakage after exposure to iRBC-egress media (Fig. 5E,F). The partial vascular barrier protective ability of AKB-9778 further highlights a crucial role of the angiopoietin-Tie axis in CM pathogenesis, as well as, suggests VE-PTP inhibition as a potential adjuvant therapeutic option for CM treatment.

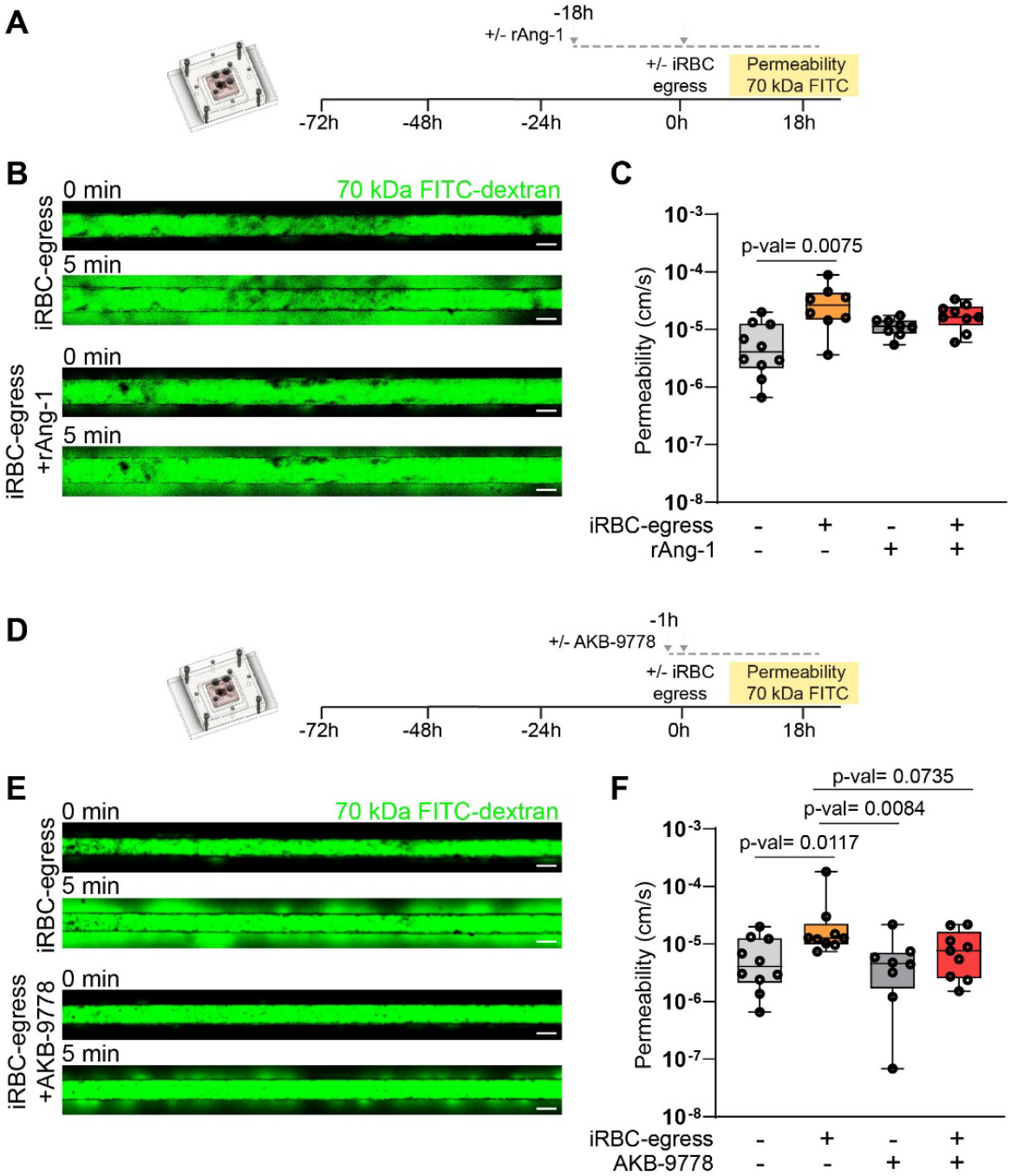

Figure 5 - Therapeutic activation of the angiopoietin-Tie axis partially protects against increased permeability induced by iRBC egress products.

A Experimental outline of the rAng-1 pre-treatment permeability experiment on 3D brain microvessels.

B Confocal image of the 70 kDa FITC-dextran flux into the surrounding collagen at 0 and 5 minutes after dextran perfusion. Images correspond to a representative iRBC-egress treated microvessel pre-treated with either media only or rAng-1 for 18 hours. Scale bars: 200 µm.

C Apparent permeability of 70 kDa FITC-dextran in microvessels pretreated with or without rAng-1 followed by 18-hour media only or iRBC-egress media treatment (n = 8-10 individual devices per condition.

D Experimental outline of the AKB-9778 pre-treatment permeability experiment on 3D brain microvessels.

E Confocal image of the 70 kDa FITC-dextran flux into the surrounding collagen at 0 and 5 minutes after dextran perfusion. Images correspond to a representative iRBC-egress treated microvessel pre-treated with either media only or AKB-9778 for 1 hour. Scale bars: 200 µm.

F Apparent permeability of 70 kDa FITC-dextran in microvessels pretreated with or without AKB-9778 followed by 18-hour media only or iRBC egress media treatment (n = 8-10 individual devices per condition).

Data information: Box and whisker plots display the median, 25th and 75th percentiles and the minimum and maximum data points in **C** and **F** (Kruskal-Wallis test corrected for multiple comparisons using the Benjamini, Krieger and Yekutieli method).

Discussion

Disruption of the angiopoietin-Tie axis is a common feature in CM patients, often associated with disease severity and fatality (Lovegrove *et al*, 2009; Conroy *et al*, 2012). This dysregulation is also found in pediatric and adult severe malaria patients without cerebral complications (Yeo *et al*, 2008; Conroy *et al*, 2009) or in placental malaria (Tran *et al*, 2021). Central to this pathway are brain pericytes, an Ang-1 secreting cell type that is located at the interface between the vasculature and brain parenchyma, yet largely understudied in the context of CM. Here, we developed a 3D brain microvessel microfluidic model that recapitulates the minimal functional brain microvascular unit to recreate the angiopoietin-Tie axis, including both primary brain microvascular endothelial cells and pericytes. Exposure of the 3D brain microvessels to *P. falciparum*-egress products caused an increase in vascular permeability accompanied by a decrease in Ang-1. Furthermore, we showed that pre-treatment with rAng-1 or the Tie-2 activator, ABK-9778, could partially protect against endothelial barrier breakdown. Taken together, these results suggest that the cessation of Ang-1 release upon exposure to iRBC-egress products is an important mechanism in microvessel disruption.

The bioengineered 3D model provides important vascular mechanical cues, including estimated flow and extracellular matrix stiffnesses present in the human brain. We could reproduce the high pericyte coverage found in the brain microvasculature by co-seeding primary brain endothelial cells

417 and pericytes through the microfluidic network. Simultaneous cell seeding, at a ratio of 5:1
418 (endothelial cells:pericytes), allowed for the formation of an intact endothelial microvessel network
419 with continuous labeling of adherens and tight junctional markers in the presence of pericytes with
420 classical cerebral pericyte marker expression. SBF-SEM microscopy showed that both cell types
421 sit at nanoscale distance, with the presence of thin lamellae extending from the pericyte soma that
422 cover large areas of the endothelium. Overall, the 3D brain microvessel model recapitulates
423 pericyte-endothelial interactions and coverage found in human brain vasculature making it suitable
424 to study the role of pericytes in CM pathogenesis.

425 *P. falciparum* products released during blood stage egress have been shown to possess barrier
426 breakdown capabilities on 2D endothelial monolayers grown on plastic. Proposed barrier disruptive
427 *P. falciparum*-iRBC egress products include merozoite proteins, histones, heme, hemozoin and *P.*
428 *falciparum* histidine rich protein 2 (Gomes *et al*, 2023; Gillrie *et al*, 2007; Gallego-Delgado *et al*,
429 2016; Pal *et al*, 2016; Storm *et al*, 2019; Moxon *et al*, 2020; Zuniga *et al*, 2022). However, their
430 effects on pericytes remain unexplored. In this study, we confirmed that these products are
431 disruptive in a microfluidics-based 3D brain microvessel model composed of primary human brain
432 endothelial cells and pericytes. Pericytes play an important role in maintaining vascular
433 homeostasis. For example, loss of pericytes from the cerebral vasculature leads to increased
434 permeability in mouse models (Armulik *et al*, 2010). Furthermore, dysregulation of cerebral
435 pericytes and detachment from the vasculature have been observed in other cerebral vasculature
436 pathologies including stroke and Alzheimer's disease (Fernández-Klett *et al*, 2013; Sengillo *et al*,
437 2013). In our study, we did not observe gross differences on pericyte morphology or loss of vascular
438 coverage upon treatment with iRBC-egress media. Nevertheless, pericytes from iRBC-egress
439 media-treated 3D microvessels did display subtle morphological changes, having significantly less
440 branches. The relevance of these minor ultrastructural modifications in vascular barrier dysfunction
441 could imply molecular mechanisms of disease. Luminex quantification upon stimulation with
442 iRBC-egress media in the 3D brain microvessel model revealed a significant reduction in N-
443 cadherin shedding. This could point towards reduced functional endothelial-pericyte interaction
444 upon short-term incubation with *P. falciparum*-egress products. Future studies should explore
445 whether exposure to *P. falciparum* for longer timepoints recapitulates phenotypes observed in post-
446 mortem samples of cerebral malaria patients such as vacuolization (Pongponratn *et al*, 2003) or
447 pericyte loss (Barrera *et al*, 2018). Nevertheless, our results point towards a loss of integrity at the
448 endothelial and pericyte interface.

449 Ang-1 and Ang-2 have been considered in the past as potential biomarkers of CM (de Jong *et al*,
450 2016). Ang-1 has excellent predictive power to distinguish malaria severity scores (Conroy *et al*,
451 2009) or malaria from other central nervous system febrile diseases (Conroy *et al*, 2010).
452 Nevertheless, the underlying mechanism of Ang-1 decrease in CM remains unknown, as previous
453 *in vitro* studies overlooked the effect that iRBC could exert on brain pericytes. To our knowledge,
454 our study is the first one to report that *P. falciparum* products released upon iRBC egress halt Ang-
455 1 secretion by pericytes. The presence of accumulated light scattering, DAPI-positive iRBC egress
456 material suggests a role of extracellular parasitic DNA or hemozoin in the cessation of Ang-1
457 secretion, yet further studies are necessary to identify the specific iRBC egress component
458 responsible for altered signaling pathways in pericytes. A complementary hypothesis for decreased
459 Ang-1 serum concentrations in CM patients is severe thrombocytopenia, commonly associated with
460 cerebral complications in *P. falciparum* infections (Sahu *et al*, 2022) since platelets are another
461 major source of serum Ang-1 (Nachman & Rafii, 2008). In light of this, it is likely that both the
462 effect of *P. falciparum*-iRBC on perivascular cells and thrombocytopenia could work in concert to
463 further contribute to a widespread decrease of Ang-1 levels. Nevertheless, our results highlight
464 brain pericytes as a new player in the development of CM through dysregulation in the secretion of
465 Ang-1.

466 Clinical studies have shown a lack of correlation between Ang-2 levels and *P. falciparum*-iRBC
467 microvascular obstruction in the rectal microvasculature (Hanson *et al*, 2015) or iRBC
468 sequestration in brain post-mortem samples (Prapansilp *et al*, 2013). Similarly, our study confirms
469 that *P. falciparum*-iRBC sequestration in 3D brain microvessel models does not directly cause Ang-
470 2 secretion by endothelial cells. This result is in concordance with a recent study that showed that
471 Ang-2 is not secreted in response to *P. falciparum* lysate products, but rather occurs following
472 endothelial activation with TNF (Gomes *et al*, 2023). Other studies have shown Ang-2 release as a
473 result of exposure to thrombin or hypoxia (Pichiule *et al*, 2004; Fiedler *et al*, 2004), conditions that
474 have also been associated with CM pathogenesis. Altogether, our study is in agreement with
475 previous reports suggesting that *P. falciparum* sequestration does not play a direct role in the
476 secretion of Ang-2, which instead is more likely a consequence of the activation of host pro-
477 inflammatory factors.

478 Modulation of the angiopoietin-Tie axis as an therapeutic target against CM has long been of
479 interest (Higgins *et al*, 2016) due to its role in strengthening endothelial tight junctions, as well as,
480 upregulating anti-apoptotic and anti-inflammatory pathways (Saharinen *et al*, 2017). Interestingly,
481 we showed that pre-incubation of human microvessels with recombinant Ang-1 protected against

482 iRBC-egress mediated barrier breakdown. While the concentration of recombinant Ang-1 utilized
483 in this study was supraphysiological compared to peripheral blood samples, it is quite likely that
484 peripheral blood concentrations underestimate local concentrations at the endothelial-pericyte
485 interface. Additionally, in our model, recombinant Ang-1 protection was only achieved after a pre-
486 incubation of 18-hours, suggesting that downstream signaling through the Tie2 receptor, such as
487 PI3K/Akt signaling, is required (Augustin *et al*, 2009).

488 Future interventions targeting the angiopoietin-Tie axis should focus on approaches that reverse
489 microvascular dysfunction after exposure to *P. falciparum.* Pre-treatment with AKB-9778 resulted
490 in rapid but partial protection against iRBC egress product-mediated breakdown, highlighting the
491 potential of the angiopoietin-Tie axis as an adjuvant therapeutic target for CM treatment.
492 Furthermore, AKB-9778-mediated activation of Tie-2 could provide an additional benefit in
493 combatting CM pathogenesis as it has also been shown to block the binding of leukocytes to the
494 vascular wall (Frye *et al*, 2015), with recent reports describing their accumulation in the brain
495 vasculature of CM patients (Riggle *et al*, 2020). Previously, Tie-2 activators such as recombinant
496 Ang-1 and the PPARγ agonist rosiglitazone have shown improved outcomes in a rodent
497 experimental CM model after onset of disease, preserving blood-brain barrier integrity, and leading
498 to a significantly increased survival rate (Higgins *et al*, 2016; Serghides *et al*, 2014). Phase II
499 clinical trials elucidating the benefit of these therapeutics in human CM treatment are currently
500 underway (Varo *et al*, 2024). Altogether, our results and others highlight the potential of
501 compounds targeting the angiopoietin-Tie2 as adjunctive CM therapies.

502 To note, our study has several limitations, including the low-throughput of the model or challenges
503 in growing the devices for long periods of time, hence preventing the modelling of long-term
504 disruptive mechanisms, such as pericyte loss. Furthermore, our devices currently represent larger
505 microvessels of the brain given the 100 μm diameter of our model and α-SMA expression on
506 pericytes. Therefore, future studies could exploit 2-photon laser ablation or bioengineered self-
507 assembled models (Arakawa *et al*, 2020; Hajal *et al*, 2022) to generate brain capillary-sized
508 microvessels (5-10 μm), a major pathogenic site in CM. Nevertheless, this study establishes a key
509 role of pericytes on microvessels that are similar in size to arterioles or post-capillary venules,
510 regions of the brain vascular tree that are equally damaged in CM patients (Barrera *et al*, 2018).
511 Finally, an additional limitation of our model is the absence of other cells that could play an
512 important role in maintaining the angiopoietin-Tie axis. For example, Ang-1 secretion has been
513 described in other brain and blood cell types, such as smooth muscle cells (Sundberg *et al*, 2002;
514 Nishishita & Lin, 2004), platelets and more recently, neurons and astrocytes (Wei *et al*, 2021). Yet,

515 one of the major advantages of *in vitro* bioengineered models is the opportunity to sequentially
516 introduce different components that, independently or collectively, could play a role in a complex
517 and multifaceted disease such as CM. Subsequent iterations of the model presented here could
518 introduce other cell types that produce Ang-1 or incorporate pro-inflammatory cytokines or
519 thrombin, to concurrently model functional consequences of increased secretion of Ang-2 by
520 endothelial cells.

521 In summary, our study highlights the role that pericytes could have in the development of CM
522 pathogenesis by showing for the first time that egress of *P. falciparum*-iRBC interrupts Ang-1
523 secretion by this cell type. In addition, our findings confirm that activation of the angiopoietin-Tie
524 axis partially protects against increased vascular permeability mediated by *P. falciparum* egress
525 products, providing further evidence that interventions involving this pathway could be part of a
526 multi-targeted adjunctive therapy against CM.

527

528 **Materials and Methods**

529 *Parasite lines:* HB3var03 variant *P. falciparum* parasites (dual ICAM-1 and EPCR binding),
530 regularly panned and monitored for appropriate PfEMP1 expression, were cultured in human B+
531 erythrocytes in RPMI 1640 medium (GIBCO) supplemented with 10% human type AB-positive
532 plasma, 5mM glucose, 0.4 mM hypoxantine, 26.8 mM sodium bicarbonate and 1.5 g/L gentamicin.
533 Parasites were grown in sealed top T75 flasks in a gas mixture of 90% N_2, 5% CO_2 and 1% O_2. To
534 maintain synchronous cultures, parasites were synchronized twice a week in their ring stage with
535 5% sorbitol and once a week in their trophozoite stage with 40 mg/mL gelaspan (Braun).

536 *P. falciparum-iRBC egress media preparation:* Late-stage *P. falciparum*-iRBC (schizonts,
537 parasitemia of 5-10%), synchronized in a 6-hour window, were purified by use of 40 mg/mL
538 gelaspan gradient separation to a final purity of >60% parasitemia. The enriched *P. falciparum*-
539 iRBC were then placed in complete RPMI media containing 1 μM compound 2, a reversible PKG
540 inhibitor that inhibits iRBC egress (kindly donated by Michael Blackman, The Francis Crick
541 Institute), at a concentration of 50 million *P. falciparum*-iRBC/mL. After 5 hours, compound 2
542 containing media was removed and the parasites were resuspended at a concentration of 100 million
543 *P. falciparum*-iRBC/mL in vascular growth media, put into a sealed top T25 flask, gassed and left
544 in the incubator overnight on a shaker set to 50 rpm to facilitate parasite egress. The resulting
545 parasite egress efficiency was assessed by a hemocytometer count and blood smear, and was then
546 concentrated to a working concentration of 50 million ruptured *P. falciparum*-iRBC/mL. The

547 resulting iRBC-egress media is spun at 1000 rpm to remove cellular debris and flash frozen in liquid
548 nitrogen until used. This concentration was chosen as this value is equivalent to a circulating
549 parasitemia of 1%, concentrations frequently found in malaria patients.

550 *Primary human brain microvascular endothelial cell and primary human brain vascular pericyte*
551 *culture:* Primary HBMEC (Cell Systems; ACBRI 376) were cultured according to the
552 manufacturer's recommendations in complete endothelial growth media-2MV (Lonza) containing
553 5% fetal bovine serum. Cells were split using Trypsin/EDTA. When 90% confluent, HBMEC were
554 seeded on 15 µg/mL Poly-L-lysine (P8920, Sigma) coated T75 flasks. Primary HBVP (ScienCell)
555 were cultured according to the manufacturer's recommendations in basal pericyte media
556 supplemented with 1% pericyte growth supplement, 1% penicillin/streptomycin and 2% fetal
557 bovine serum (ScienCell). Cells were split using Trypsin/EDTA when 90% confluent, seeded on
558 15 µg/mL Poly-L-lysine coated T75 flasks, and maintained in a humidified incubator at 37 °C and
559 5% CO_2. All experiments were conducted with HBMEC and HBVP with a passage number of 7-9.

560 *mCherry lentivirus transduction:* HBVPs were grown in a T75 flask to a ~90% confluency and
561 incubated with lentiviral particles containing a mCherry vector (kindly donated by Kristina Haase
562 Lab, EMBL Barcelona) in serum free pericyte media at a multiplicity of infection of 10. After 24
563 hours, the lentivirus particles were removed by washing once every 24-hours for a 2-day period.
564 mCherry-positive cells were then selected by fluorescence-activated cell sorting, expanded and
565 froze down for future experiments.

566 *3D brain microvessel model fabrication:* Type 1 collagen was extracted from rat tails, dissolved in
567 0.1% acetic acid, lyophilized in a freezer dryer (Labconco Freezone 2.5 Plus) and resuspended at
568 15 mg/mL in 0.1% acetic acid for storage. The stock collagen solution-0.1% acetic acid solution
569 was neutralized and diluted to 7.5 mg/mL on ice. A 13 by 13 channel grid or single channel pattern
570 were negatively imprinted into the collagen hydrogel by soft lithography using a PDMS stamp, and
571 inlet and outlets were created by insertion of stainless-steel dowel pins. The top pre-patterned
572 collagen hydrogel contained in a plexiglass top jig is sealed to a flat collagen-layered bottom that
573 sits on a coverslip and a plexiglass bottom jig. The assembly creates perfusable 120 µm diameter
574 microvessels (grid design) or 200 µm diameter microvessels (single channel design), as described
575 previously (Zheng *et al*, 2012; Piatti *et al*, 2022). Prior to cell seeding, the channels were incubated
576 with vascular growth media, consisting in EGM-2MV (Lonza) supplemented with 1x pericyte and
577 1x astrocyte growth factors (ScienCell) for 1 hour. Primary HBMECs and HBVPs, or mCherry-
578 positive HBVPs (for pericyte coverage analysis), were resuspended at concentrations of 7 million
579 cells/mL and mixed to a ratio of 5:1 HBMECs to HBVPs. The cell mixture was then seeded into

580 the inlet in 8 μL increments and driven through the microfluidic network by gravity-driven flow.
581 Cells were perfused twice from either the inlet or outlet until the channels were completely covered
582 with adhered cells. Media was then removed and devices were flipped upside down for 1-hour to
583 ensure even cell distribution on the top and bottom of the channels. Microvessels were cultured for
584 3 days before being used in experiments with media change every twice per day by gravity driven
585 flow.

586 *Immunofluorescence microscopy:* Microvessel labeling was performed by gravity driven flow.
587 Microvessels were fixed with 3.7% paraformaldehyde (PFA) in PBS for 15 minutes followed by
588 three 10-minute washes with PBS. Next microvessels were incubated with Background Buster
589 (Innovex) for 30 minutes and then permeabilized with blocking buffer (0.1% Triton X-100 and 2%
590 bovine serum albumin in phosphate-buffered saline (PBS)). Primary antibodies including rabbit
591 anti-αSMA-555 (EPR5368, Abcam), mouse anti-vWF (sc-365712, Santa Cruz), mouse anti-ZO-1
592 (Invitrogen, 10017242), rabbit anti-β-catenin (Cell Signaling, 9587S), mouse anti-PDGFRβ
593 (Abcam, ab69506), mouse anti-NG-2 (Invitrogen, 10424493), rabbit anti-laminin (Abcam,
594 ab11575), rabbit anti-collagen IV (Abcam, ab6586)), mouse anti-VE-cadherin (sc-52751, Santa
595 Cruz), and Phalloidin-647 (Invitrogen, A22287) were diluted in blocking buffer at 1:100 and
596 incubated overnight at 4 °C. After three 10-minute PBS washes, secondary antibodies including
597 goat anti-mouse Alexa Fluor 488 (A11001, Invitrogen), goat anti-rabbit Alexa Fluor 488
598 (Invitrogen, A-11008), goat anti-mouse Alexa Fluor 594 (Invitrogen, A-11005), goat anti-rabbit
599 Alexa Fluor 594 (Invitrogen, A-11012), goat anti-mouse Alexa Fluor 647 (A21235, Invitrogen),
600 goat anti-rabbit Alexa Fluor 647 (Invitrogen, A-21244) and 2 mg/mL DAPI (D21490, Invitrogen)
601 were diluted at 1:250 in 2% bovine serum albumin and 5% goat serum containing PBS, and
602 incubated at room temperature for 1 hour. Microvessels were washed 6 times with PBS for 10
603 minutes each and then imaged on a Zeiss LSM 980 Airyscan 2. Image stacks were acquired with 3
604 μm or 10 μm z-step size for single or tile scan images respectively. Z-projections and further
605 threshold analysis was done using Fiji (ImageJ v1.54f) software.

606 *Pericyte coverage analysis:* Tile scan images of the microvessel network with mCherry-positive
607 HBVP and vWF-labeled HBMEC were acquired as described above. Images were divided into two
608 stacks, one being the top half of the microvessels of the network and the other the bottom half.
609 Next, Z-projections of the top and bottom surfaces of the network were generated. The percentage
610 of endothelial surface that was covered by pericytes was calculated by creating a mask of both the
611 mCherry HBVP and the vWF-positive HBMEC.

612 *Serial Block-Face Scanning Electron Microscopy:* Microvessel devices were grown for 3 days,
613 then treated with iRBC-egress media or vascular growth media for 18hours, and then fixed by
614 adding 2% PFA and 2.5% glutaraldehyde (GA) to the device inlet for 30-minutes and washed twice
615 with EGM-2MV at 37 °C. The collagen hydrogel was then carefully removed from the plexiglass
616 jig and microvessel regions exposed to low shear stress were cut out and fixed with a secondary
617 fixative solution (2% PFA, 2.5% GA, 0.25 mM $CaCl_2$, 0.5 mM MgCl, 5% sucrose in a pH 7.4 0.1
618 M Cacodylate buffer) overnight at 4 °C, and then rinsed twice for 15-minutes with 0.1 M
619 Cacodylate buffer. Samples were post-fixed in a reduced Osmium solution (1% OsO_4, 1.5%
620 K_3FeCN_6 in 0.065 M Cacodylate buffer) for 2-hours at 4 °C followed by six 10-minute washes in
621 dH_2O. Post-staining consisted of subsequent incubation steps of 1% thiocarbohydrazide in dH_2O,
622 2% Osmium tetroxide in dH_2O, and 1% Uranyl acetate in dH_2O, aided by a PELCO Biowave Pro+
623 (Ted Pella) containing a SteadyTemp Pro and ColdSpot set to 20 °C at 7x 2 minute cycling on-off
624 at 100 W under vacuum, with dH_2O rinses in between steps once in a fume hood and twice in the
625 microwave at 250 W for 40 s without vacuum. The stained samples were then dehydrated by serial
626 additions of 30, 50, 80, and 100% ethanol solutions in the microwave at 250 W for 40 s without
627 vacuum with ColdSpot set to 4 °C, infiltrated with EPON 812 hard epoxy resin in steps of 25, 50,
628 75, 90, and 3x 100% resin diluted in ethanol with each step in the microwave at 150 W for 3 minutes
629 under vacuum and polymerized at 60 °C for 48 hours. The sample was trimmed (UC7, Leica
630 Microsystems) using a 90° cryo-trimmer (Diatome) to generate a small block face. The resulting
631 resin block was mounted on a pin stub using silver conductive epoxy resin (Ted Pella). The SBF-
632 SEM acquisition was performed with a Zeiss Gemini2 equipped with a Gatan 3view microtome
633 and a focal charge compensation device (Zeiss). The SEM was operated at 1.5 kV 300 pA, using a
634 pixel size of 15 nm, a slice thickness of 50 nm and a dwell time of 1.6 µs. The SBF-SEM acquisition
635 was performed using the software SBEMimage (Titze *et al*, 2018). The acellular center of the lumen
636 was not imaged to save imaging time. Following acquisition, the positional metadata of the sections
637 and tiles obtained was converted with SBEM-specific import scripts
638 (https://git.embl.de/schorb/rendermodules-addons) for subsequent assembly, stitching and
639 alignment of large EM datasets (Mahalingam *et al*, 2022). Aligned images were then binned to 22
640 by 22 by 250 nm^3 in xyz and segmentation was then performed using the software package Amira
641 (Thermo Fischer Scientific). Primary HBVP and HBMEC were segmented semi manually using
642 the magic wand and brush tool to segment every fifth section followed by use of the interpolation
643 tool to segment the entire volume. The resulting segmented microvessels were rendered using the
644 generate surfaces module for 3D visualization.

645 *P. falciparum-iRBC and iRBC-egress media perfusion to 3D brain microvessels:* All experiments
646 were done in 3D microvessel devices grown for 3 days. Schizont-stage *P. falciparum*-iRBC were
647 purified to >60% parasitemia by 40 mg/mL gelaspan and the resulting enriched population was
648 diluted in vascular growth media to 50 million iRBC/mL (same concentration as the *P. falciparum*-
649 iRBC-egress media). 200 µL of *P. falciparum*-iRBC or *P. falciparum*-iRBC-egress media was
650 added into the device inlet and perfused by gravity flow for 30-minutes with the outlet effluent
651 being reintroduced to the inlet every 10 minutes. Microvessels treated with intact *P. falciparum*-
652 iRBC (but not *P. falciparum*-iRBC-egress media), were then washed for 10 minutes with vascular
653 growth media. Both conditions were incubated overnight for 18 hours. Supernatant was then
654 removed from the outlet and pooled for Luminex analysis, and 3D brain microvessels were used
655 for permeability studies or fixed for imaging with 3.7% PFA for 15-minutes (see section
656 immunofluorescence microscopy).

657 *Fluorescent dextran-based permeability assay:* Single channel microvessel devices were grown for
658 3 days, then perfused and incubated for 18 hours with either vascular growth media or *P.*
659 *falciparum*-iRBC-egress media as described above. To determine resulting changes in
660 permeability, they were perfused with a 70 kDa FITC-dextran solution as follows: the device was
661 washed 1x with PBS and placed in a Zeiss LSM 980 Airyscan2 confocal microscope with a
662 temperature and CO_2 controlled imaging chamber (37 °C, 5% CO_2). PBS was aspirated and 100 µL
663 of 70 kDa FITC-dextran solution (100 µg/mL) in PBS was pulled from the inlet to the outlet at 6.5
664 µL/min flow rate using a syringe pump (Harvard Apparatus PHD 2000). Tilescan confocal images
665 of the entire channel were taken every 30 seconds for 5 minutes once the channel had been filled
666 with FITC dextran. In devices pre-treated with 1 µg/mL recombinant Ang-1 (923-AB-025, R&D
667 Systems), pre-incubation occurred at 18-hours, starting on day 2. In devices pre-treated with 10 µM
668 AKB-9778 (HY-1009041-1MG, MedChemExpress), pre-incubation occurred 1 hour prior to
669 iRBC-egress media or media addition.

670 *Quantification of apparent permeability:* Apparent permeability is determined as the flux of
671 fluorescently labeled dextran across the microvessel wall into the surrounding collagen hydrogel.
672 All steps of permeability analysis were performed using ImageJ. By using the following equation:

673 $$Papp = \frac{1}{I_{Vt1} - I_{Tt1}} \times \frac{I_{Tt2} - I_{Tt1}}{\Delta t} \times \frac{A_{\text{lateral tissue}}}{P}$$

674 The apparent permeability (P_{app}) was calculated using the fluorescence intensity inside the vessel
675 (I_V) and in the surrounding collagen hydrogel (I_T) at two time points t1 (0 minutes after the vessel
676 is filled with dextran) and t2 (5 minutes after the vessel is filled). Δt is the change in time, $A_{lateral}$

677 $_{tissue}$ is the area of the collagen hydrogel being examined and P is the perimeter of the microvessel.
678 To account for *P. falciparum*-iRBC-egress material that appears dark even in the presence of 70
679 kDa FITC-dextran, regions of *P. falciparum*-iRBC-egress material were excluded from the
680 calculation of the fluorescence intensity inside the vessel (I_V) by using ImageJ median smoothing
681 and the magic wand tool to select only the area of the channel without *P. falciparum*-iRBC-egress
682 material.

683 *Serial Block-Face Scanning Electron Microscopy pericyte morphology analysis:* 3D-rendered
684 pericyte meshes, segmented from SBF-SEM images of microvessels treated with either media alone
685 or iRBC-egress media, were generated using Amira. Following segmentation, the meshes were
686 exported as *STL* files and processed with a custom-developed Python script, designed to quantify
687 aspects of pericyte morphology, including mesh circularity and maximum width (waleedmirzaPhD,
688 2024). Firstly, the 3D pericyte meshes were mapped onto a 2D plane through principal component
689 analysis (PCA), effectively reducing the data's dimensionality while retaining its most significant
690 morphological features. This mapping uses the two principal components that encapsulate the
691 dimensions with the maximum variance in the 3D mesh, thus ensuring the conservation of structural
692 information. Subsequently, convex hull analysis (Virtanen *et al*, 2020) was applied to delineate the
693 pericyte mesh boundaries, providing a clear representation of each structure's shape by which
694 circularity and maximum width could be measured. The circularity of each mesh is calculated using
695 the convex hull, by assessing the ratio of the area enclosed by the hull to the square of the hull
696 perimeter, with the formula for circularity given as $4\pi \times Area/Perimeter^2$. This circularity
697 metric provides insight into the roundness of the mesh, where a value closer to 1 indicates a shape
698 that is more circular, and values closer to 0 reflect more elongated or irregular shapes. Additionally,
699 the maximum width is defined by identifying the two farthest points along the convex hull boundary
700 and then calculating the greatest perpendicular distance from this line (connecting the farthest
701 points) to any point within the convex hull. This measurement represents the maximum width of
702 the pericyte mesh by assuming its length is the axis with the greater size. In addition, the number
703 of pericyte branches was calculated manually by counting the number of branches on each 3D
704 rendered pericyte.

705 *Co-culture transwell fabrication:* 10^5 HBVPs were seeded on the basolateral side of Poly-L-lysine
706 treated transwell inserts (12 well PET membrane inserts with a pore size of 3 μm) in 100 μL of
707 media and left to attach for 4-6 hours. Transwell inserts were then flipped into a 12 well culture
708 plate containing 1200 μL of pericyte media and allowed to grow for 2 days. Next, 10^5 HBMECs
709 were seeded onto the apical side of the Poly-L-lysine treated transwell inserts in 300 μL of media

710 and left to attach for 4-6 hours. Then media was removed from both sides of the insert and 1200 µL
711 of pericyte media was added to the basolateral side and 800 µL of EGM-2MV media to the apical
712 side. The cells were allowed to grow for 2 more days. On day 5, supernatants were taken from the
713 basolateral side for angiopoietin-1 ELISA. Endothelial cell-only transwells underwent the same
714 fabrication protocol minus the initial pericyte steps.

715 *Angiopoietin-1 ELISA:* Ang-1 protein concentrations were measured from supernatants taken from
716 the basolateral side of the transwell model. Supernatant concentrations were obtained by running
717 5X diluted samples on either the Human Angiopoietin-1 DuoSet ELISA kit (DY923, R&D
718 Systems). Protein concentrations were interpolated from sigmoidal 4-parameter-fit standard curves
719 generated from a 7-point standard curve of recombinant human proteins using GraphPad Prism.
720

721 *Quantification of secreted proteins by Luminex Assay:* Secreted protein concentrations were
722 measured from supernatants taken from the outlets of 3D brain microvessels with a 13 x 13 grid
723 geometry. Supernatants from 2-3 devices exposed to the same condition were pooled, diluted 2X
724 and assayed using a 10-plex Human Luminex Discovery Assay from R&D Systems on a Luminex
725 100/200. The 10-plex panel included: Ang-1, Ang-2, PDGF-BB, N-cadherin, TIMP-1, ANGPTL4,
726 VEGF, Tie-2, IL-8, and CXCL-1. Protein concentrations were interpolated from a 11-point standard
727 curve of known concentrations of recombinant human proteins provided by the vendor and reported
728 as pg/mL using xPONENT 4.2. 7 out of 10 analytes were in the standard curve quantification range
729 for 100% of measurements recorded, with Timp-1, N-cadherin and IL-8 having 100% of
730 measurements above the upper limit of quantification.

731 *Measuring changes in barrier integrity by xCELLigence:* 96 well PET E-plates (300600910,
732 Agilent) were coated with 15 µg/mL Poly-L-lysine and 5000 HBMECs in 200 µL EGM-2MV were
733 added per well. After cell adherence, the plate was placed into the xCELLigence RTCA SP reader
734 to begin baseline measurement of growth-related changes in cell index (an arbitrary measure of
735 impedance) and the cells were incubated for 3 days until cell index reached a plateau (indicative of
736 cell confluence). Media was changed every two days. For initial testing of the impact of iRBC-
737 egress media on barrier integrity, on the day of the experiment iRBC-egress media was added at
738 concentrations of either 12.5, 25 or 50 million ruptured iRBC/mL. Changes in cell index were
739 measured every 15-seconds for 8 hours and then every 15-minutes for 48-hours. To test the impact
740 of rAng-1 or AKB-9778 on barrier breakdown mediated by *P. falciparum*-iRBC-egress, iRBC-
741 egress media was added at $50x10^6$ ruptured iRBC/mL after either a 1- or 18-hour pre-incubation
742 with 1 µg/mL of rAng-1 or 10 µM of AKB-9778. Again, changes in cell index were measured every

743 15 seconds for 8 hours and then every 15-minutes for 48-hours. Quantification of partial protection
744 was done by first normalizing each condition to the media only control. Then the area under the
745 curve of the negative values, indicative of barrier breakdown, was calculated using GraphPad Prism
746 (version 10.0.2) where the media only without rAng-1 condition represented an average value of 0
747 and the iRBC-egress media without rAng-1 condition an average value of 100.

748 *Statistical analysis:*All statistics were obtained by use of GraphPad Prism (version 10.0.2). Non-
749 parametric Mann-Whitney U tests were performed for most experiments, except to calculate Ang-
750 1 protection in the 2D xCELLigence and microvessel experiments in which a repeated measures
751 one-way ANOVA test with Dunnett's multiple comparisons test and Kruskal-Wallis test with
752 Dunn's multiple comparisons test were performed respectively. A P-value<0.05 was considered
753 statistically significant.

754 **Author contributions**

755 R.L and M.B conceived the work. R.L, P.R, R.A, and M.B designed experiments. R.L performed
756 most experiments with assistance of F.K, P.R, H.F, M.M, and R.A. R.L, P.R, H.F, W.M, R.A, Y.S,
757 G.M, M.B analyzed the data. R.L and M.B wrote the original draft of the manuscript. All authors
758 contributed to manuscript writing, revision, editing and suggestions.

759 **Acknowledgements**

760 We want to thank Kristina Haase (EMBL Barcelona) for her support and careful suggestions on the
761 project and manuscript writing, as well as for assistance with the generation of mCherry HBVP
762 with help from Violeta Beltran-Sastre. We acknowledge access to the CRG/UPF flow cytometry
763 facility for mCherry HBVP sorting. We are grateful to Carlota Dobaño (ISGlobal) for access to the
764 Luminex and to Michael Blackman (The Francis Crick Institute) who kindly gifted compound 2.
765 This work was facilitated by the EMBL Electron Microscopy Core Facility (EMCF), with important
766 assistance from Viola Oorschot on sample preparation and processing, and Karel Mocaer and
767 Martin Schorb on image analysis. The great majority of this work was supported by the core
768 program funding of the European Molecular Biology Laboratory (EMBL) and the European
769 Research Council (ERC) under the European Union's Horizon 2020 research and innovation
770 program (Grant agreement no. 948088). F.K is funded through the Marie Skłodowska-Curie grant
771 agreement (101068552). H.F is supported by a fellowship from the EMBL Interdisciplinary
772 (EI4POD) program under Marie Skłodowska-Curie Actions COFUND (847543). G.M. is supported
773 by RYC 2020–029886 I/ AEI/10.13039/501100011033, co funded by European Social Fund (ESF).

ISGlobal received support from the grant CEX2018-000806-S funded by MCIN/AEI/ 10.13039/501100011033, and support from the Generalitat de Catalunya through the CERCA Program. This research is part of the ISGlobal's Program on the Molecular Mechanisms of Malaria which is partially supported by the Fundación Ramón Areces.

Bibliography

Arakawa C, Gunnarsson C, Howard C, Bernabeu M, Phong K, Yang E, DeForest CA, Smith JD & Zheng Y (2020) Biophysical and biomolecular interactions of malaria-infected erythrocytes in engineered human capillaries. *Sci Adv* 6: eaay7243

Armulik A, Genové G, Mäe M, Nisancioglu MH, Wallgard E, Niaudet C, He L, Norlin J, Lindblom P, Strittmatter K, *et al* (2010) Pericytes regulate the blood–brain barrier. *Nature* 468: 557–561

Attwell D, Mishra A, Hall CN, O'Farrell FM & Dalkara T (2016) What is a pericyte? *J Cereb Blood Flow Metab* 36: 451–455

Augustin HG, Young Koh G, Thurston G & Alitalo K (2009) Control of vascular morphogenesis and homeostasis through the angiopoietin–Tie system. *Nat Rev Mol Cell Biol* 10: 165–177

Barrera V, MacCormick IJC, Czanner G, Hiscott PS, White VA, Craig AG, Beare NAV, Culshaw LH, Zheng Y, Biddolph SC, *et al* (2018) Neurovascular sequestration in paediatric P. falciparum malaria is visible clinically in the retina. *eLife* 7: e32208

Bernabeu M, Gunnarsson C, Vishnyakova M, Howard CC, Nagao RJ, Avril M, Taylor TE, Seydel KB, Zheng Y & Smith JD (2019) Binding Heterogeneity of Plasmodium falciparum to Engineered 3D Brain Microvessels Is Mediated by EPCR and ICAM-1. *mBio* 10: e00420-19

Bernabeu M & Smith JD (2017) EPCR and Malaria Severity: The Center of a Perfect Storm. *Trends in Parasitology* 33: 295–308

Birbeck GL, Molyneux ME, Kaplan PW, Seydel KB, Chimalizeni YF, Kawaza K & Taylor TE (2010) Blantyre Malaria Project Epilepsy Study (BMPES) of neurological outcomes in retinopathy-positive paediatric cerebral malaria survivors: a prospective cohort study. *The Lancet Neurology* 9: 1173–1181

Conroy AL, Glover SJ, Hawkes M, Erdman LK, Seydel KB, Taylor TE, Molyneux ME & Kain KC (2012) Angiopoietin-2 levels are associated with retinopathy and predict mortality in Malawian children with cerebral malaria: A retrospective case–control study*. *Critical Care Medicine* 40: 952

Conroy AL, Lafferty EI, Lovegrove FE, Krudsood S, Tangpukdee N, Liles WC & Kain KC (2009) Whole blood angiopoietin-1 and -2 levels discriminate cerebral and severe (non-cerebral) malaria from uncomplicated malaria. *Malaria Journal* 8: 295

Conroy AL, Phiri H, Hawkes M, Glover S, Mallewa M, Seydel KB, Taylor TE, Molyneux ME & Kain KC (2010) Endothelium-Based Biomarkers Are Associated with Cerebral Malaria in Malawian Children: A Retrospective Case-Control Study. *PLOS ONE* 5: e15291

Daneman R & Prat A (2015) The Blood–Brain Barrier. *Cold Spring Harb Perspect Biol* 7: a020412

Denk W & Horstmann H (2004) Serial Block-Face Scanning Electron Microscopy to Reconstruct Three-Dimensional Tissue Nanostructure. *PLOS Biology* 2: e329

813 Dondorp AM, Fanello CI, Hendriksen IC, Gomes E, Seni A, Chhaganlal KD, Bojang K, Olaosebikan R,
814 Anunobi N, Maitland K, *et al* (2010) Artesunate versus quinine in the treatment of severe
815 falciparum malaria in African children (AQUAMAT): an open-label, randomised trial. *The Lancet*
816 376: 1647–1657

817 Dorovini-Zis K, Schmidt K, Huynh H, Fu W, Whitten RO, Milner D, Kamiza S, Molyneux M & Taylor
818 TE (2011) The Neuropathology of Fatal Cerebral Malaria in Malawian Children. *The American*
819 *Journal of Pathology* 178: 2146–2158

820 Fernández-Klett F, Potas JR, Hilpert D, Blazej K, Radke J, Huck J, Engel O, Stenzel W, Genové G &
821 Priller J (2013) Early Loss of Pericytes and Perivascular Stromal Cell-Induced Scar Formation
822 after Stroke. *J Cereb Blood Flow Metab* 33: 428–439

823 Fiedler U, Scharpfenecker M, Koidl S, Hegen A, Grunow V, Schmidt JM, Kriz W, Thurston G & Augustin
824 HG (2004) The Tie-2 ligand Angiopoietin-2 is stored in and rapidly released upon stimulation
825 from endothelial cell Weibel-Palade bodies. *Blood* 103: 4150–4156

826 Frye M, Dierkes M, Küppers V, Vockel M, Tomm J, Zeuschner D, Rossaint J, Zarbock A, Koh GY, Peters
827 K, *et al* (2015) Interfering with VE-PTP stabilizes endothelial junctions in vivo via Tie-2 in the
828 absence of VE-cadherin. *Journal of Experimental Medicine* 212: 2267–2287

829 Fukuhara S, Sako K, Minami T, Noda K, Kim HZ, Kodama T, Shibuya M, Takakura N, Koh GY &
830 Mochizuki N (2008) Differential function of Tie2 at cell–cell contacts and cell–substratum
831 contacts regulated by angiopoietin-1. *Nat Cell Biol* 10: 513–526

832 Gallego-Delgado J, Basu-Roy U, Ty M, Alique M, Fernandez-Arias C, Movila A, Gomes P, Weinstock A,
833 Xu W, Edagha I, *et al* (2016) Angiotensin receptors and β-catenin regulate brain endothelial
834 integrity in malaria. *Journal of Clinical Investigation* 126: 4016–4029

835 Gillrie MR, Krishnegowda G, Lee K, Buret AG, Robbins SM, Looareesuwan S, Gowda DC & Ho M
836 (2007) Src-family kinase–dependent disruption of endothelial barrier function by Plasmodium
837 falciparum merozoite proteins. *Blood* 110: 3426–3435

838 Golledge J, Clancy P, Maguire J, Lincz L, Koblar S, McEvoy M, Attia J, Levi C, Sturm J, Almeida OP, *et*
839 *al* (2014) Plasma Angiopoietin-1 Is Lower After Ischemic Stroke and Associated With Major
840 Disability But Not Stroke Incidence. *Stroke* 45: 1064–1068

841 Gomes C, Varo R, Duran-Frigola M, Sitoe A, Bila R, Machevo S, Mayor A, Bassat Q & Rodriguez A
842 (2023) Endothelial transcriptomic analysis identifies biomarkers of severe and cerebral malaria.
843 *JCI Insight* 8

844 Grant RI, Hartmann DA, Underly RG, Berthiaume A-A, Bhat NR & Shih AY (2019) Organizational
845 hierarchy and structural diversity of microvascular pericytes in adult mouse cortex. *J Cereb Blood*
846 *Flow Metab* 39: 411–425

847 Gurnik S, Devraj K, Macas J, Yamaji M, Starke J, Scholz A, Sommer K, Di Tacchio M, Vutukuri R, Beck
848 H, *et al* (2016) Angiopoietin-2-induced blood–brain barrier compromise and increased stroke size
849 are rescued by VE-PTP-dependent restoration of Tie2 signaling. *Acta Neuropathol* 131: 753–773

850 Haase K, Gillrie MR, Hajal C & Kamm RD (2019) Pericytes Contribute to Dysfunction in a Human 3D
851 Model of Placental Microvasculature through VEGF-Ang-Tie2 Signaling. *Advanced Science* 6:
852 1900878

853 Hajal C, Offeddu GS, Shin Y, Zhang S, Morozova O, Hickman D, Knutson CG & Kamm RD (2022)
854 Engineered human blood–brain barrier microfluidic model for vascular permeability analyses. *Nat*
855 *Protoc* 17: 95–128

856 Hanson J, Lee SJ, Hossain MA, Anstey NM, Charunwatthana P, Maude RJ, Kingston HWF, Mishra SK,
857 Mohanty S, Plewes K, *et al* (2015) Microvascular obstruction and endothelial activation are
858 independently associated with the clinical manifestations of severe falciparum malaria in adults: an
859 observational study. *BMC Medicine* 13: 122

860 He L, Vanlandewijck M, Raschperger E, Andaloussi Mäe M, Jung B, Lebouvier T, Ando K, Hofmann J,
861 Keller A & Betsholtz C (2016) Analysis of the brain mural cell transcriptome. *Sci Rep* 6: 35108

862 Higgins SJ, Purcell LA, Silver KL, Tran V, Crowley V, Hawkes M, Conroy AL, Opoka RO, Hay JG,
863 Quaggin SE, *et al* (2016) Dysregulation of angiopoietin-1 plays a mechanistic role in the
864 pathogenesis of cerebral malaria. *Sci Transl Med* 8: 358ra128

865 Howard C, Joof F, Hu R, Smith JD & Zheng Y (2023) Probing cerebral malaria inflammation in 3D
866 human brain microvessels. *Cell Reports* 42: 113253

867 Jain V, Lucchi NW, Wilson NO, Blackstock AJ, Nagpal AC, Joel PK, Singh MP, Udhayakumar V, Stiles
868 JK & Singh N (2011) Plasma levels of angiopoietin-1 and -2 predict cerebral malaria outcome in
869 Central India. *Malar J* 10: 383

870 de Jong GM, Slager JJ, Verbon A, van Hellemond JJ & van Genderen PJJ (2016) Systematic review of the
871 role of angiopoietin-1 and angiopoietin-2 in Plasmodium species infections: biomarkers or
872 therapeutic targets? *Malaria Journal* 15: 581

873 Kessler A, Dankwa S, Bernabeu M, Harawa V, Danziger SA, Duffy F, Kampondeni SD, Potchen MJ,
874 Dambrauskas N, Vigdorovich V, *et al* (2017) Linking EPCR-Binding PfEMP1 to Brain Swelling
875 in Pediatric Cerebral Malaria. *Cell Host & Microbe* 22: 601-614.e5

876 Lovegrove FE, Tangpukdee N, Opoka RO, Lafferty EI, Rajwans N, Hawkes M, Krudsood S,
877 Looareesuwan S, John CC, Liles WC, *et al* (2009) Serum Angiopoietin-1 and -2 Levels
878 Discriminate Cerebral Malaria from Uncomplicated Malaria and Predict Clinical Outcome in
879 African Children. *PLOS ONE* 4: e4912

880 Mahalingam G, Torres R, Kapner D, Trautman ET, Fliss T, Seshamani S, Perlman E, Young R, Kinn S,
881 Buchanan J, *et al* (2022) A scalable and modular automated pipeline for stitching of large electron
882 microscopy datasets. *eLife* 11: e76534

883 Maisonpierre PC, Suri C, Jones PF, Bartunkova S, Wiegand SJ, Radziejewski C, Compton D, McClain J,
884 Aldrich TH, Papadopoulos N, *et al* (1997) Angiopoietin-2, a Natural Antagonist for Tie2 That
885 Disrupts in vivo Angiogenesis. *Science* 277: 55–60

886 Mathiisen TM, Lehre KP, Danbolt NC & Ottersen OP (2010) The perivascular astroglial sheath provides a
887 complete covering of the brain microvessels: An electron microscopic 3D reconstruction. *Glia* 58:
888 1094–1103

889 Mohanty S, Benjamin LA, Majhi M, Panda P, Kampondeni S, Sahu PK, Mohanty A, Mahanta KC,
890 Pattnaik R, Mohanty RR, *et al* (2017) Magnetic Resonance Imaging of Cerebral Malaria Patients
891 Reveals Distinct Pathogenetic Processes in Different Parts of the Brain. *mSphere* 2:
892 10.1128/msphere.00193-17

893 Moxon CA, Alhamdi Y, Storm J, Toh JMH, McGuinness D, Ko JY, Murphy G, Lane S, Taylor TE, Seydel
894 KB, *et al* (2020) Parasite histones are toxic to brain endothelium and link blood barrier breakdown
895 and thrombosis in cerebral malaria. *Blood Adv* 4: 2851–2864

896 Nachman RL & Rafii S (2008) Platelets, Petechiae, and Preservation of the Vascular Wall. *New England*
897 *Journal of Medicine* 359: 1261–1270

898 Nahirney PC, Reeson P & Brown CE (2016) Ultrastructural analysis of blood–brain barrier breakdown in
899 the peri-infarct zone in young adult and aged mice. *J Cereb Blood Flow Metab* 36: 413–425

900 Nishishita T & Lin PC (2004) Angiopoietin 1, PDGF-B, and TGF-β gene regulation in endothelial cell and
901 smooth muscle cell interaction. *Journal of Cellular Biochemistry* 91: 584–593

902 Oliveira F, Bondareva O, Rodríguez-Aguilera JR & Sheikh BN (2023) Cultured brain pericytes adopt an
903 immature phenotype and require endothelial cells for expression of canonical markers and ECM
904 genes. *Front Cell Neurosci* 17

905 Ornelas S, Berthiaume A-A, Bonney SK, Coelho-Santos V, Underly RG, Kremer A, Guérin CJ, Lippens S
906 & Shih AY (2021) Three-dimensional ultrastructure of the brain pericyte-endothelial interface. *J*
907 *Cereb Blood Flow Metab* 41: 2185–2200

908 Pal P, Daniels BP, Oskman A, Diamond MS, Klein RS & Goldberg DE (2016) Plasmodium falciparum
909 Histidine-Rich Protein II Compromises Brain Endothelial Barriers and May Promote Cerebral
910 Malaria Pathogenesis. *mBio* 7: 10.1128/mbio.00617-16

911 Peddie CJ, Genoud C, Kreshuk A, Meechan K, Micheva KD, Narayan K, Pape C, Parton RG, Schieber
912 NL, Schwab Y, *et al* (2022) Volume electron microscopy. *Nat Rev Methods Primers* 2: 51

913 Piatti L, Howard CC, Zheng Y & Bernabeu M (2022) Binding of Plasmodium falciparum-Infected Red
914 Blood Cells to Engineered 3D Microvessels. In *Malaria Immunology*, Jensen ATR & Hviid L
915 (eds) pp 557–585. New York, NY: Springer US

916 Pichiule P, Chavez JC & LaManna JC (2004) Hypoxic Regulation of Angiopoietin-2 Expression in
917 Endothelial Cells*. *Journal of Biological Chemistry* 279: 12171–12180

918 Pongponratn E, Turner GDH, Day NPJ, Phu NH, Simpson JA, Stepniewska K, Mai NTH, Viriyavejakul P,
919 Looareesuwan S, Hien TT, *et al* (2003) An ultrastructural study of the brain in fatal Plasmodium
920 falciparum malaria. *Am J Trop Med Hyg* 69: 345–359

921 Prapansilp P, Medana I, Mai NTH, Day NP, Phu NH, Yeo TW, Hien TT, White NJ, Anstey NM & Turner
922 GD (2013) A clinicopathological correlation of the expression of the angiopoietin-Tie-2 receptor
923 pathway in the brain of adults with Plasmodium falciparum malaria. *Malaria Journal* 12: 50

924 Riggle BA, Manglani M, Maric D, Johnson KR, Lee M-H, Neto OLA, Taylor TE, Seydel KB, Nath A,
925 Miller LH, *et al* (2020) $CD8^+$ T cells target cerebrovasculature in children with cerebral malaria. *J*
926 *Clin Invest* 130: 1128–1138

927 Saharinen P, Eklund L & Alitalo K (2017) Therapeutic targeting of the angiopoietin-TIE pathway. *Nat Rev*
928 *Drug Discov* 16: 635–661

929 Saharinen P, Eklund L, Miettinen J, Wirkkala R, Anisimov A, Winderlich M, Nottebaum A, Vestweber D,
930 Deutsch U, Koh GY, *et al* (2008) Angiopoietins assemble distinct Tie2 signalling complexes in
931 endothelial cell–cell and cell–matrix contacts. *Nat Cell Biol* 10: 527–537

932 Sahu PK, Duffy FJ, Dankwa S, Vishnyakova M, Majhi M, Pirpamer L, Vigdorovich V, Bage J, Maharana
933 S, Mandala W, *et al* (2022) Determinants of brain swelling in pediatric and adult cerebral malaria.
934 *JCI Insight* 6

935 Sengillo JD, Winkler EA, Walker CT, Sullivan JS, Johnson M & Zlokovic BV (2013) Deficiency in Mural
936 Vascular Cells Coincides with Blood–Brain Barrier Disruption in Alzheimer's Disease. *Brain*
937 *Pathology* 23: 303–310

938 Serghides L, McDonald CR, Lu Z, Friedel M, Cui C, Ho KT, Mount HTJ, Sled JG & Kain KC (2014)
939 PPARγ Agonists Improve Survival and Neurocognitive Outcomes in Experimental Cerebral
940 Malaria and Induce Neuroprotective Pathways in Human Malaria. *PLoS Pathog* 10: e1003980

941 Siddiqui MR, Mayanil CS, Kim KS & Tomita T (2015) Angiopoietin-1 Regulates Brain Endothelial
942 Permeability through PTPN-2 Mediated Tyrosine Dephosphorylation of Occludin. *PLOS ONE* 10:
943 e0130857

944 Smyth LCD, Rustenhoven J, Scotter EL, Schweder P, Faull RLM, Park TIH & Dragunow M (2018)
945 Markers for human brain pericytes and smooth muscle cells. *Journal of Chemical Neuroanatomy*
946 92: 48–60

947 Storm J, Jespersen JS, Seydel KB, Szestak T, Mbewe M, Chisala NV, Phula P, Wang CW, Taylor TE,
948 Moxon CA, *et al* (2019) Cerebral malaria is associated with differential cytoadherence to brain
949 endothelial cells. *EMBO Molecular Medicine* 11: e9164

950 Sundberg C, Kowanetz M, Brown LF, Detmar M & Dvorak HF (2002) Stable Expression of Angiopoietin-
951 1 and Other Markers by Cultured Pericytes: Phenotypic Similarities to a Subpopulation of Cells in
952 Maturing Vessels During Later Stages of Angiogenesis *In Vivo*. *Laboratory Investigation* 82: 387–
953 401

954 Titze B, Genoud C & Friedrich RW (2018) SBEMimage: Versatile Acquisition Control Software for Serial
955 Block-Face Electron Microscopy. *Front Neural Circuits* 12

956 Tran V, Weckman AM, Crowley VM, Cahill LS, Zhong K, Cabrera A, Elphinstone RE, Pearce V,
957 Madanitsa M, Kalilani-Phiri L, *et al* (2021) The Angiopoietin-Tie2 axis contributes to placental
958 vascular disruption and adverse birth outcomes in malaria in pregnancy. *eBioMedicine* 73

959 Uemura MT, Maki T, Ihara M, Lee VMY & Trojanowski JQ (2020) Brain Microvascular Pericytes in
960 Vascular Cognitive Impairment and Dementia. *Front Aging Neurosci* 12

961 Varo R, Crowley VM, Mucasse H, Sitoe A, Bramugy J, Serghides L, Weckman AM, Erice C, Bila R,
962 Vitorino P, *et al* (2024) Adjunctive rosiglitazone treatment for severe pediatric malaria: A
963 randomized placebo-controlled trial in Mozambican children. *International Journal of Infectious*
964 *Diseases* 139: 34–40

965 Virtanen P, Gommers R, Oliphant TE, Haberland M, Reddy T, Cournapeau D, Burovski E, Peterson P,
966 Weckesser W, Bright J, *et al* (2020) SciPy 1.0: fundamental algorithms for scientific computing in
967 Python. *Nat Methods* 17: 261–272

968 waleedmirzaPhD (2024) waleedmirzaPhD/cell_analysis_toolkit.

969 Wassmer SC, de Koning-Ward TF, Grau GER & Pai S (2024) Unravelling mysteries at the perivascular
970 space: a new rationale for cerebral malaria pathogenesis. *Trends in Parasitology* 40: 28–44

971 Wei X, Jessa S, Kleinman CL & Phoenix TN (2021) Mapping Angiopoietin1 Expression in the
972 Developing and Adult Brain. *Developmental Neuroscience* 43: 321–334

973 Yeo TW, Lampah DA, Gitawati R, Tjitra E, Kenangalem E, Piera K, Price RN, Duffull SB, Celermajer DS
974 & Anstey NM (2008) Angiopoietin-2 is associated with decreased endothelial nitric oxide and
975 poor clinical outcome in severe falciparum malaria. *Proceedings of the National Academy of*
976 *Sciences* 105: 17097–17102

977 Zheng Y, Chen J, Craven M, Choi NW, Totorica S, Diaz-Santana A, Kermani P, Hempstead B, Fischbach-
978 Teschl C, López JA, *et al* (2012) In vitro microvessels for the study of angiogenesis and
979 thrombosis. *Proceedings of the National Academy of Sciences* 109: 9342–9347

980 Zuniga M, Gomes C, Chen Z, Martinez C, Devlin JC, Loke P & Rodriguez A (2022) Plasmodium
981 falciparum and TNF-α Differentially Regulate Inflammatory and Barrier Integrity Pathways in
982 Human Brain Endothelial Cells. *mBio* 13: e01746-22

983
984

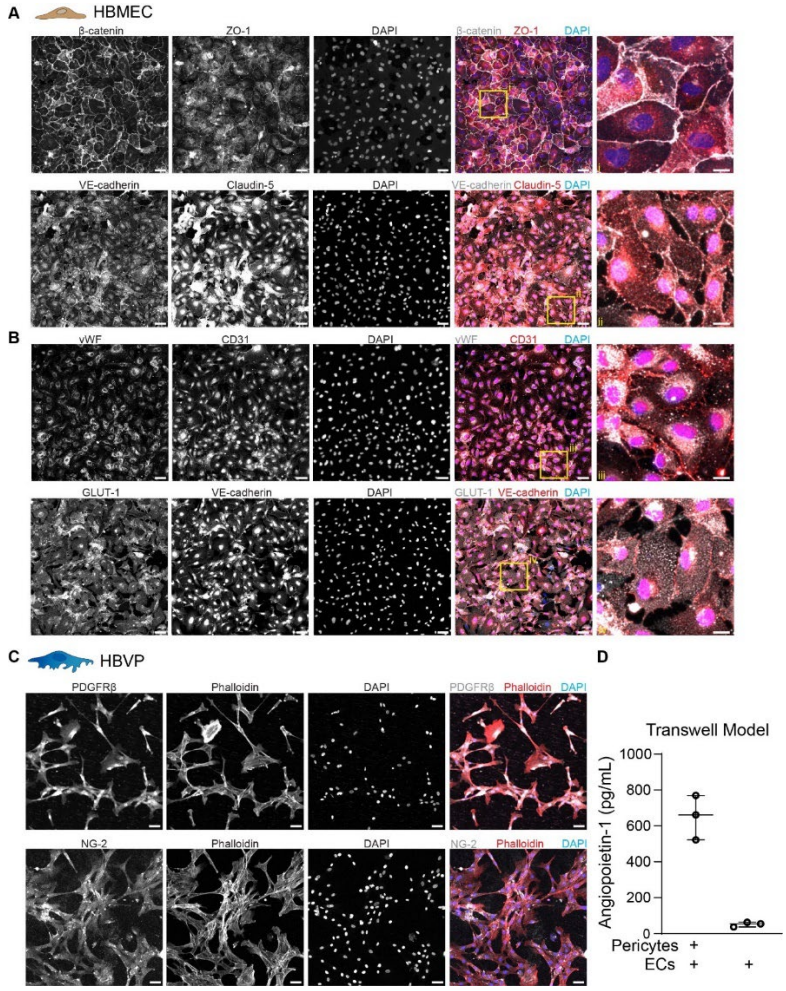

Figure EV1 - Characterization of brain-specific endothelial and pericyte marker expression and secretion of angiopoietin-Tie axis components.

A Immunofluorescence maximum z-projection of a 2D HBMEC monolayer stained for adherens and tight junctional markers: β-catenin, VE-cadherin, ZO-1 (top) and Claudin-5 (bottom), and 4', 6-diamidino-2-phenylindole (DAPI). The merged image includes the adherens junction markers (white), tight junction markers (red) and DAPI labeling (blue). Scale bars: 50 µm and 10 µm for the insets.

B Immunofluorescence maximum z-projection of a 2D HBMEC monolayer stained for vWF, brain glucose transporter GLUT-1, CD31, VE-cadherin and DAPI. The merge image includes vWF or GLUT-1 (white), CD31 or VE-cadherin (red) and DAPI labeling (blue). Insets in A and B display zoomed merge region of interests (ROIs) to better highlight the cellular localization of each marker. Scale bars: 50 µm and 10 µm for the insets.

C Immunofluorescence maximum z-projection of a 2D HBVP monolayer stained for PDGFRβ (top) and NG-2 (bottom), Phalloidin and DAPI. The merge staining includes the pericyte markers (white), phalloidin (red) and DAPI labeling (blue). Scale bars: 50 µm.

D Concentration of secreted angiopoietin-1 in supernatant obtained from either HBVP-HBMEC co-culture or HBMEC-only monolayers grown in a transwell model. (n = 3 independent experiments.

Data information: Box and whisker plots display the median and the minimum and maximum data points.

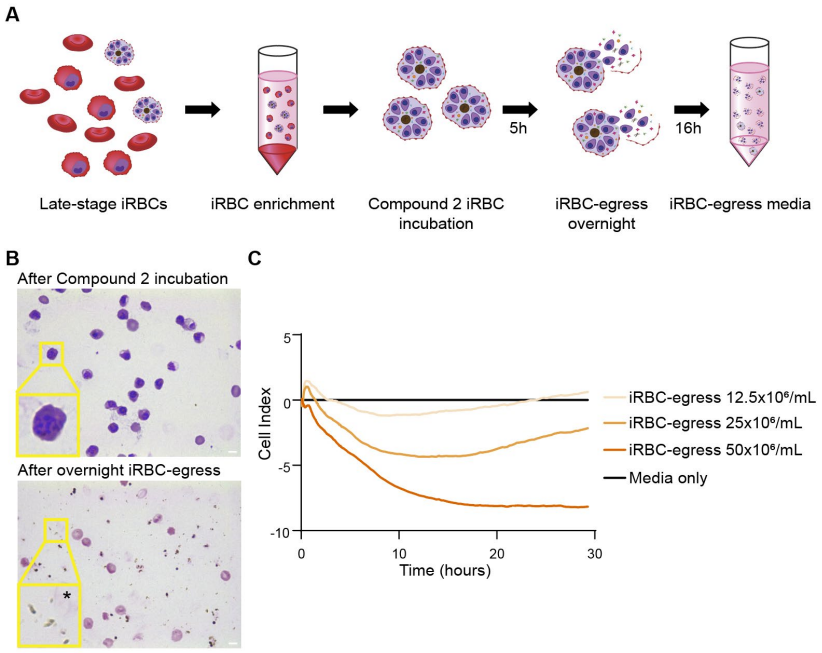

Figure EV2 - Generation of endothelial barrier disruptive iRBC-egress media.
A Schematic representation of the protocol to make iRBC-egress media. In short, late-stage *P. falciparum*-iRBC are purified by a gelaspan gradient separation and then incubated for 5 hours with compound-2 to synchronize them at the point of egress. Compound-2 is removed and the *P. falciparum*-iRBC are resuspended in vascular growth media and left overnight on a shaker at 50 rpm to egress.
B A thin smear of tightly synchronized schizonts before the removal of Compound-2 (yellow inset highlights a ROI with a schizont-stage iRBC) or the resultant iRBC-egress media before centrifugation (yellow inset highlights a ROI with free hemazoin particles next to an iRBC ghost, denoted with an asterisk) stained with giemsa. Scale bars: 5 µm.
C Representative recording data of xCELLigence measurements on 2D HBMEC monolayers in the absence of HBVP taken after addition of iRBC-egress media at different concentrations. Data is normalized to the media-only control.

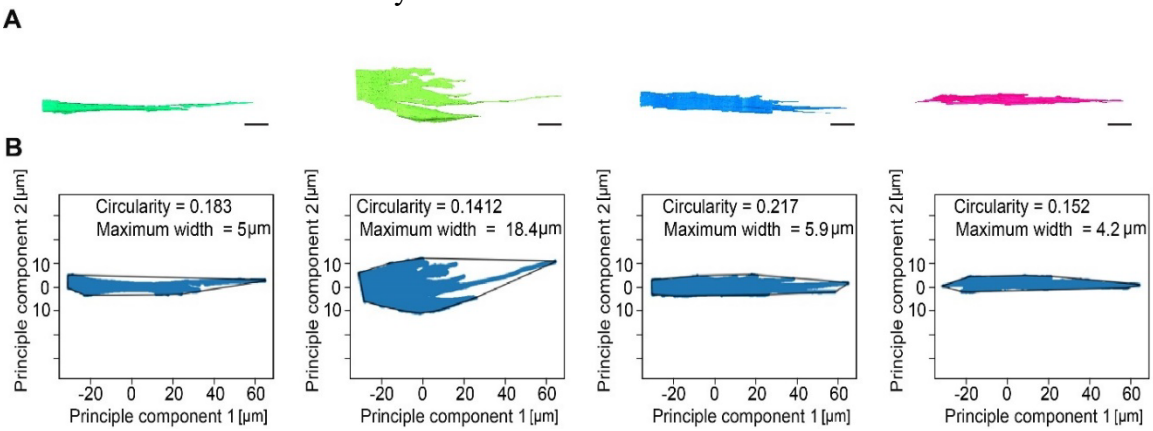

Figure EV3 - Analysis of pericyte morphological features.
A The analysis pipeline begins with the extraction of 3D segmented pericyte meshes. Shown here are four representative pericytes. Scale bars: 10 µm.
B Pericyte geometry is flattened into two principal dimensions using PCA by a Python-based image analysis pipeline. The 2D geometry's shape is then determined using convex hull analysis. To describe pericyte morphology, pericyte cell borders are analyzed for circularity, calculated as 4π*Area/Perimeter^2, where a value of 1 indicates a perfect circle and values approaching 0 indicate increasingly elongated shapes, and maximum width.

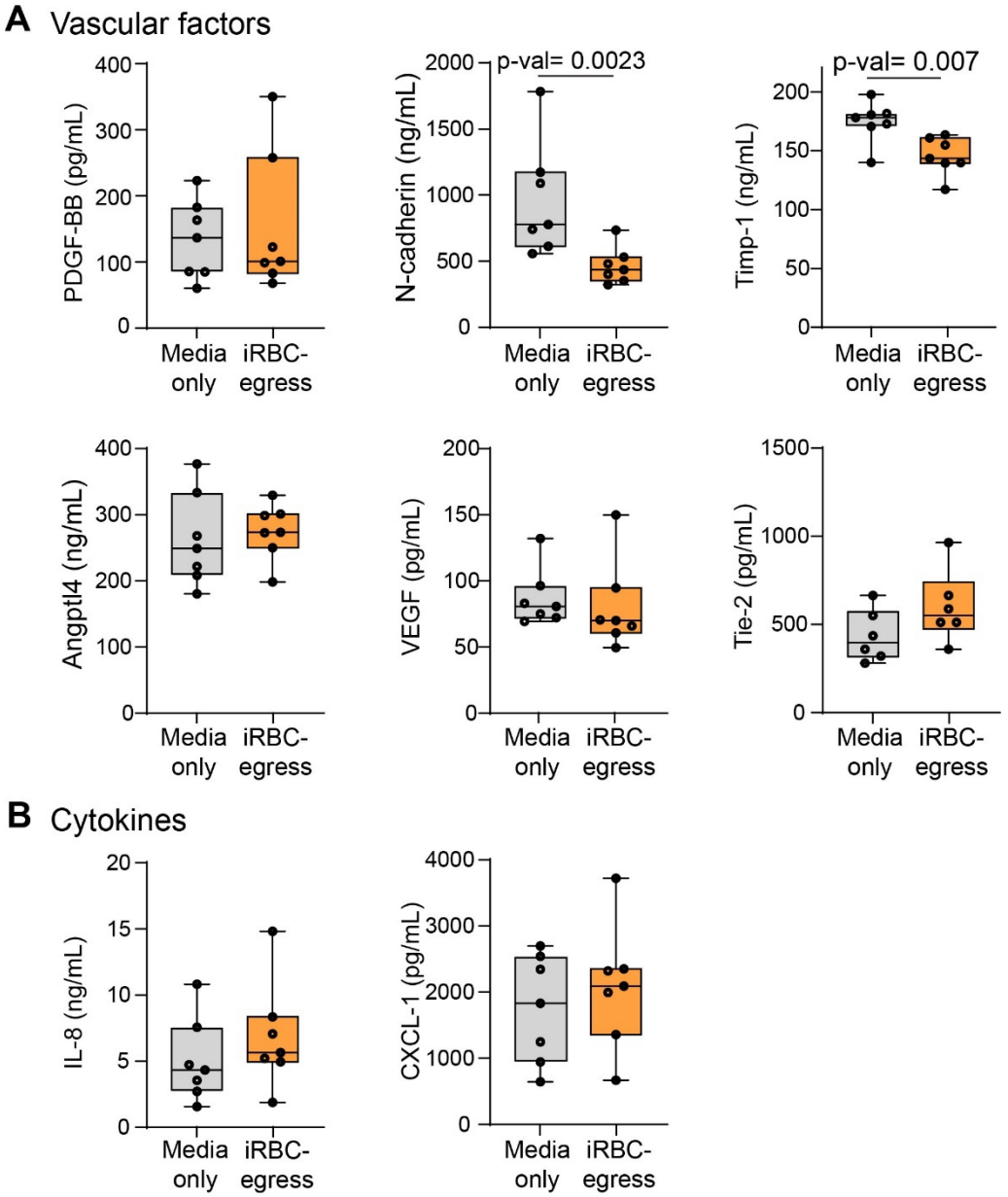

Figure EV4 - iRBC egress products cause alteration of endothelial cell-pericyte interaction markers.

A Concentrations of vascular factors PDGF-BB, N-cadherin, Timp-1, Angptl4, VEGF and Tie-2 measured by Luminex from 3D brain microvessels supernatants treated with media only or iRBC-egress media for 18-hours. Box and whisker plots display the median, 25th and 75th percentiles and the minimum and maximum data points. (n_= 7 supernatants pooled from 2-3 devices each).

B Concentrations of released cytokines IL-8 and CXCL-1 measured by Luminex from 3D brain microvessels supernatants treated with media only or iRBC-egress media for 18-hours. Box and whisker plots display the median, 25th and 75th percentiles and the minimum and maximum data points. (n_= 7 supernatants pooled from 2-3 devices each).

Data information: Statistical significance is analyzed by Mann-Whitney U test (**A** and **B**).

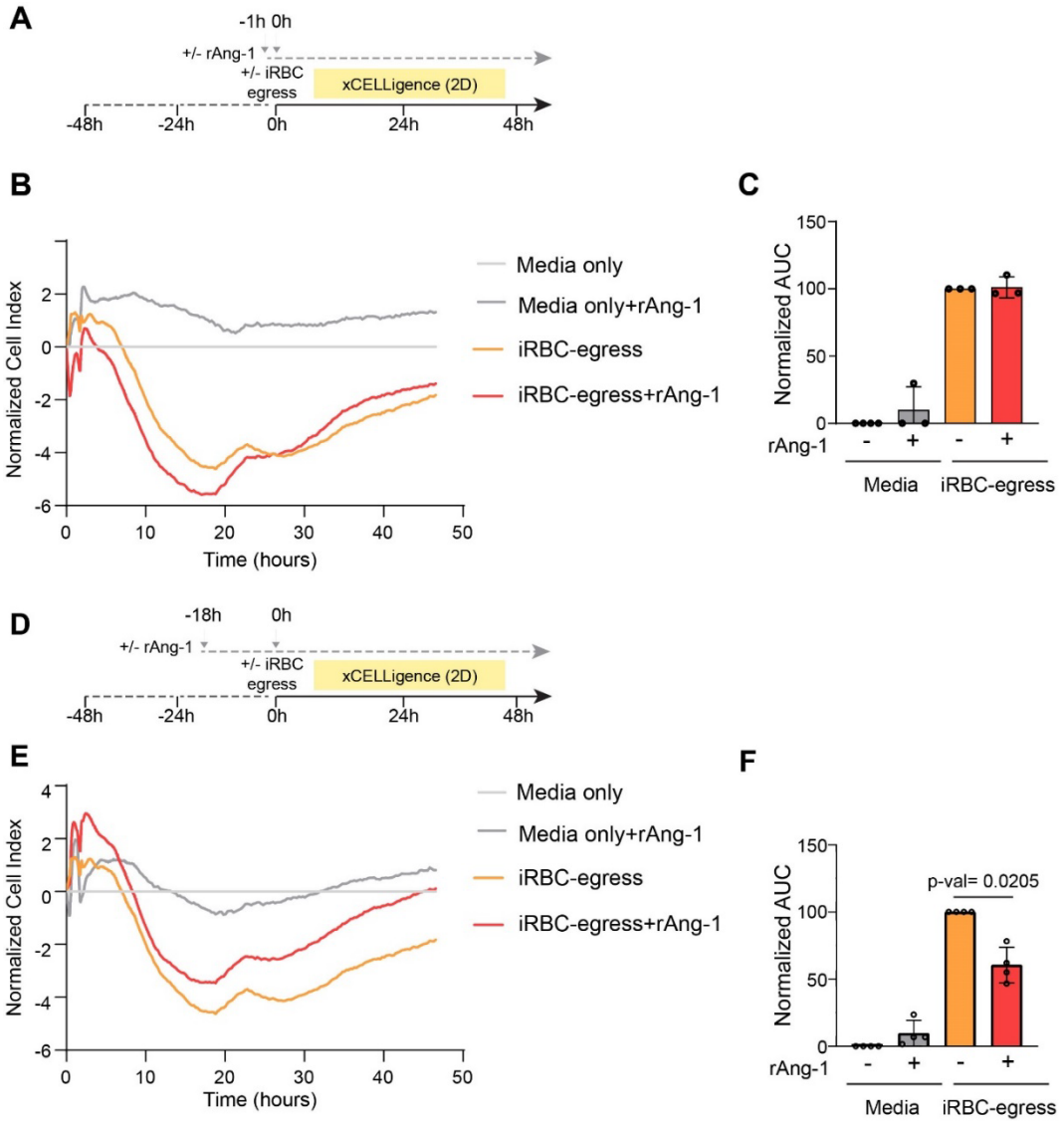

Figure EV5 - 18-hour recombinant Ang-1 pre-treatment partially protects against 2D endothelial monolayer permeability increase induced by iRBC egress products.

A Experimental outline of short-term (1-hour) incubation with rAng-1 in a 2D HBMEC monolayer in the absence of HBVP.

B Representative recording data of xCELLigence measurements taken after a 1-hour +/-rAng-1 pre-treatment followed by +/- iRBC-egress media addition. All conditions were normalized to the media only control.

C Area under the curve analysis of with iRBC-egress media normalized as 100 (n = 3 independent experiments run in triplicate).

D Experimental outline of long-term (18-hour) incubation with rAng-1 in a 2D HBMEC monolayer in the absence of HBVP.

E Representative recording data of xCELLigence measurements taken after an 18-hour +/- rAng-1 pre-treatment followed by +/- iRBC-egress media addition. All conditions were normalized to the media only control.

F Area under the curve analysis of 4 independent experiments run in triplicate with iRBC-egress media normalized as 100. (n = 4 independent experiments run in triplicate).

Data information: Error bars represent mean +/- standard deviation. Statistical significance is measured by repeated measures one-way ANOVA test with Dunnett's multiple comparisons test (**C** and **F**).

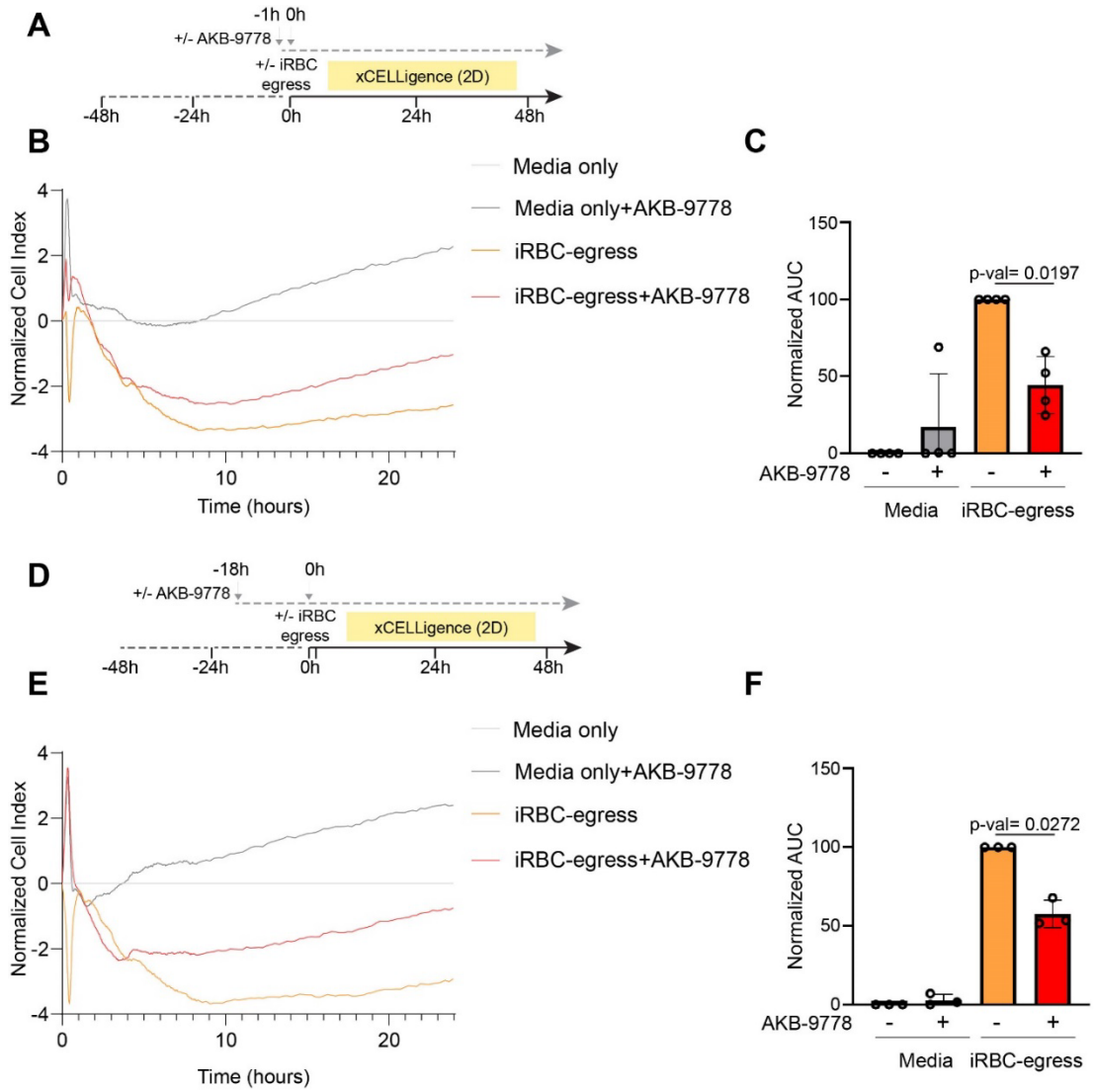

Figure EV6 - 1- and 18-hour AKB-9778 pre-treatment partially protects against 2D endothelial monolayer permeability increase induced by iRBC egress products.

A Experimental outline of short-term (1-hour) incubation with AKB-9778 in a 2D HBMEC monolayer in the absence of HBVP.

B Representative recording data of xCELLigence measurements taken after a 1-hour +/-AKB-9778 pre-treatment followed by +/- iRBC-egress media addition. All conditions were normalized to the media only control.

C Area under the curve analysis with iRBC-egress media normalized as 100 (n= of 4 independent experiments run in triplicate).

D Experimental outline of long-term (18-hour) incubation with AKB-9778 in a 2D HBMEC monolayer in the absence of HBVP.

E Representative recording data of xCELLigence measurements taken after an 18-hour +/- rAng-1 pre-treatment followed by +/- iRBC-egress media addition. All conditions were normalized to the media only control.

F Area under the curve analysis with iRBC-egress media normalized as 100. (n = 3 independent experiments run in triplicate).

Data information: Error bars represent mean +/- standard deviation. Statistical significance is measured by repeated measures one-way ANOVA test with Dunnett's multiple comparisons test (**C** and **F**).